AD-A074 070   COMPUTATIONAL MECHANICS CONSULTANTS INC KNOXVILLE TN   F/G 20/4
                   A NUMERICAL VISCOUS-INVISCID INTERACTION ALGORITHM FOR PREDICTI--ETC(U)
                   FEB 79   A J BAKER, P D MANHARDT   N62269-77-C-0491
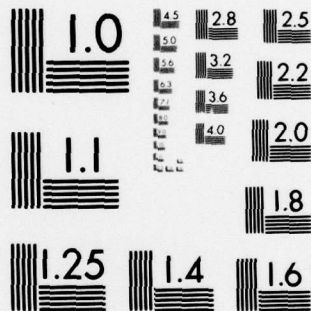UNCLASSIFIED   NADC-77167-30   NL

| OF |
AD
A074070

MICROCOPY RESOLUTION TEST CHART

NATIONAL BUREAU OF STANDARDS-1963-A

LEVEL

A NUMERICAL VISCOUS-INVISCID INTERACTION

ALGORITHM FOR PREDICTION OF NEAR-FIELD

VSTOL JET-INDUCED FLOWFIELDS

By

A. J. Baker

&

P. D. Manhardt

Computational Mechanics Consultants, Inc.

3601A Chapman Highway

Knoxville, TN   37920

February   1979

Contract N62269-77C-0491

Report NADC-77167-30

Prepared for

Naval Air Development Center

Warminster, PA 18974

79 09 18 151

REPORT DOCUMENTATION PAGE		READ INSTRUCTIONS BEFORE COMPLETING FORM
1. REPORT NUMBER NADC-77167-30	2. GOVT ACCESSION NO.	3. RECIPIENT'S CATALOG NUMBER
4. TITLE (and Subtitle) A Numerical Viscous-Inviscid Interaction Algorithm for Prediction of Near-Field VSTOL Jet-Induced Flowfields.		5. TYPE OF REPORT & PERIOD COVERED FINAL REPORT 10/77-9/78
		6. PERFORMING ORG. REPORT NUMBER
7. AUTHOR(s) A. J. Baker and P. D. Manhardt		8. CONTRACT OR GRANT NUMBER(s) N62269-77C-0491
9. PERFORMING ORGANIZATION NAME AND ADDRESS Computational Mechanics Consultants 3601A Chapman Highway Knoxville, Tennessee 37920		10. PROGRAM ELEMENT, PROJECT, TASK AREA & WORK UNIT NUMBERS
11. CONTROLLING OFFICE NAME AND ADDRESS Naval Air Development Center (3015) Warminster, Pennsylvania 18974		12. REPORT DATE February, 1979
		13. NUMBER OF PAGES 72
14. MONITORING AGENCY NAME & ADDRESS(If different from Controlling Office)		15. SECURITY CLASS. (of this report) UNCLASSIFIED
		15a. DECLASSIFICATION/DOWNGRADING SCHEDULE

16. DISTRIBUTION STATEMENT (of this Report)

Approved for public release; distribution unlimited.

17. DISTRIBUTION STATEMENT (of the abstract entered in Block 20, If different from Report)

18. SUPPLEMENTARY NOTES

19. KEY WORDS (Continue on reverse side if necessary and identify by block number)

VSTOL
Three-Dimensional Interaction
Turbulent Flow

Finite Element
Computer Program
Jet/Crosswind

20. ABSTRACT (Continue on reverse side if necessary and identify by block number)

A turbulent-inviscid numerical interaction algorithm is derived and evaluated for detailed determination of the near-field flow of a jet injected perpendicular to a crosswind. The two distinct solution domains are pressure coupled through a Poisson equation solution, and entrainment-induced mass flux is an iteration variable. Finite element procedures are employed for solution of the resulting non-linear initial-boundary value equations. Key results are discussed documenting viability for analysis of a round-jet at a velocity ratio equal to eight.

DD FORM 1473 EDITION OF 1 NOV 65 IS OBSOLETE
1 JAN 73
S/N 0102-014-6601 |

PREFACE

The research effort reported herein was performed by Computational
Mechanics Consultants, Inc. during the period October 1977 through
September 1978 with Dr. A. J. Baker as Principal Investigator. The
sponsorship was provided by the Naval Air Development Center, Warminster,
PA, under contract No. N62269-77-C-0491. The NADC technical monitor was
Dr. K. T. Yen, whose helpful suggestions and experienced guidance are
acknowledged.

A NUMERICAL VISCOUS-INVISCID INTERACTION

ALGORITHM FOR PREDICTION OF NEAR-FIELD

VSTOL JET-INDUCED FLOWFIELDS

By

A. J. Baker and P. D. Manhardt

Computational Mechanics Consultants, Inc.

3601A Chapman Highway

Knoxville, TN 37920

SUMMARY

A viscous-inviscid interaction algorithm has been derived for numerical determination of the detailed three-dimensional flowfield surrounding and entrained into the wake of a V/STOL jet issued orthogonally into a subsonic crossflow bounded on one plane by an aerodynamic surface. The dominant influence parameter coupling the three-dimensional external potential flow analysis, and the imbedded three-dimensional viscous and turbulent analysis of the jet and nearfield-wake, is the entrainment flow induced into the jet region and its influence on the potential flow. The two distinct solution domains are pressure coupled, and the entrainment-induced mass flux addition to the wake is the primary iteration variable of the global algorithm.

A key element of the algorithm is definition of a surface defining the coincident boundary of the dual analyses. Numerical studies have confirmed existence of the interface surface for the test case of a circular jet issued into a crossflow with velocity ratio equal to eight. This determination yields definition of the specific geometry of the interface intersection with the injection plane and the entrainment velocity distribution thereon. Available experimental surface pressure data are specifically employed in this analysis phase, and available additional data are used to complete definition of the interface surface evolution. The summary three-dimensional jet region computations yield determination of the detailed evolution of the turbulent flow and employs a turbulence closure model involving all six components of the Reynolds stress tensor. Finite element numerics have been employed to computationally evaluate the five distinct computational phases of the algorithm.

TABLE OF CONTENTS

LIST OF SYMBOLS

a	boundary condition coefficient
b	body force
c	isentropic sound speed; coefficient
C	coefficient; airfoil chord
d	differential; jet diameter
e	finite element index
f	function of known argument; coordinate curve
g	function; source term
h	metric coefficient; integration step size
H	stagnation enthalpy
k	turbulence kinetic energy; interpolation polynomial degree
K	generalized diffusion coefficient
ℓ	differential operator; length scale
L	differential operator
M	number of finite elements spanning R^n
n	unit normal vector; dimensionality
N	finite element cardinal basis
p	pressure; generalized parameter; iteration index
q	generalized dependent variable
Q	generalized discretized dependent variable
R	domain of elliptic operator
Re	Reynolds number
S	finite element assembly operator
t	time
T	temperature

u_i	velocity vector
U	reference velocity
x_i	Cartesian coordinate system
α	parameter
∂R	closure of solution domain R^n
δ	Kronecker delta; increment; trailing edge included angle
δ^*	boundary layer displacement thickness
Δ	increment; element measure
ϵ	turbulence dissipation function
η_i	transformed coordinate system
ξ_i	transformed coordinate system
κ	karman coefficient
λ	jet velocity ratio; multiplier
μ	dynamic viscosity
ν	kinematic viscosity; general diffusion coefficient
ρ	density
σ_{ij}	mean flow Stokes stress tensor
τ	Reynolds stress tensor
ϕ	velocity potential function
χ	generalized initial-value operator
Ω	global solution domain

Superscripts:

e	effective value
I	inviscid flow reference
n	dimension of R

o	initial condition
t	turbulent
T	matrix transpose
+	turbulence correlation function
~	mass-weighted time-average
——	time average
^	unit vector
´	mass-weighted fluctuating component; ordinary derivative

Subscripts:

∞	global reference condition
e	finite element domain
i,j,k,ℓ	tensor indices
j	jet reference
-	non-tensor index
n	normal
o	initial condition
t	time derivative

Notation:

{ }	column matrix
[ ]	square matrix
$\cup$	union
$\cap$	intersection
ε	belongs to
| |	absolute value

LIST OF FIGURES

INTRODUCTION

In the transition from hover to wing-borne flight, a significant
fraction of the lift of a V/STOL aircraft is furnished by direct engine
thrust. This injection of a high-velocity jet of exhaust (or air) at almost
right angles to the aerodynamic surface and to the cross-flow induced by
the aircraft forward flight, produces an extremely complicated three-
dimensional local flowfield which can significantly alter the aircraft aero-
dynamic characteristics. Since the basic phenomena of transverse jet
injection is so fundamental to V/STOL performance, it is crucially important
that a firm understanding of cause and effect be established. The mission
of this research project is to derive, implement and computationally evaluate
the key features of a three-dimensional viscous-inviscid flow interaction
numerical solution algorithm for the near-field of a V/STOL jet.

Since the transverse injected jet is fundamental to many physical
processes, in addition to V/STOL aircraft, a comprehensive base of experi-
mental data and linearized theoretical analyses has become established.
Perhaps the first consequential theoretical study was reported in the disser-
tation of Chang (ref. 1), who employed potential flow theory and bound vortex
filament concepts to predict roll-up of the separation boundary between a
parallel onset flow and a perpendicular cylindrical jet. A series expansion
solution yielded the prediction of the initial roll-up near the jet exit
plane illustrated in Figure 1. A (hand) numerical solution predicted the
further-field roll-up shown in Figure 2, which clearly illustrates evolution
to the hallmark horse-shoe cross-sectional shape. This basic concept
(application of potential flow theory) has been expanded upon and refined to
a great extent, and has produced (viscous-corrected) models of the V/STOL jet
that can accurately predict gross jet flow parameters such as jet centerline
trajectory, lateral spread, cross-section shape and mean axial velocity at
each cross-section (c.f., ref. 2, 3).

The earliest analyses showed only the potential flow aspect of the
interaction of the two flows while current models employ empirical corrections
to approximate the dominant viscous effects such as "entrainment." Jordinson
(ref. 4) conducted early experiments on a round jet that confirmed the horse-
shoe cross-section contours, and also noted that the jet drew the flow boundary
layer up into the jet wake region. This is not a dominant feature of a jet
issued from an isolated pipe (ref. 5), and has become recognized as perhaps
a most consequential contributor to performance alterations of V/STOL aircraft.
Entrainment is properly interpreted as the total effect of vortex roll-up plus
the induced turbulent mixing, while blockage is simply the characteristics for
inviscid flow around an equivalent solid body. The potential flow model
equivalent is therefore a cylinder with suction coupled with an empirical
accounting for viscous effects.

The significant interest in the V/STOL jet problem prompted the conducting
of many comprehensive experimental test projects to probe the associated three-
dimensional velocity fields to well downstream of injection and to record
induced surface pressure distributions. It is this later phenomenon that is
perhaps the singularly important analysis requirement since in practice the
injection plate becomes a (lifting) aerodynamic surface. Vogler (ref. 6),
Bradbury and Wood, (ref. 7) published early results. McMahan and Mosher
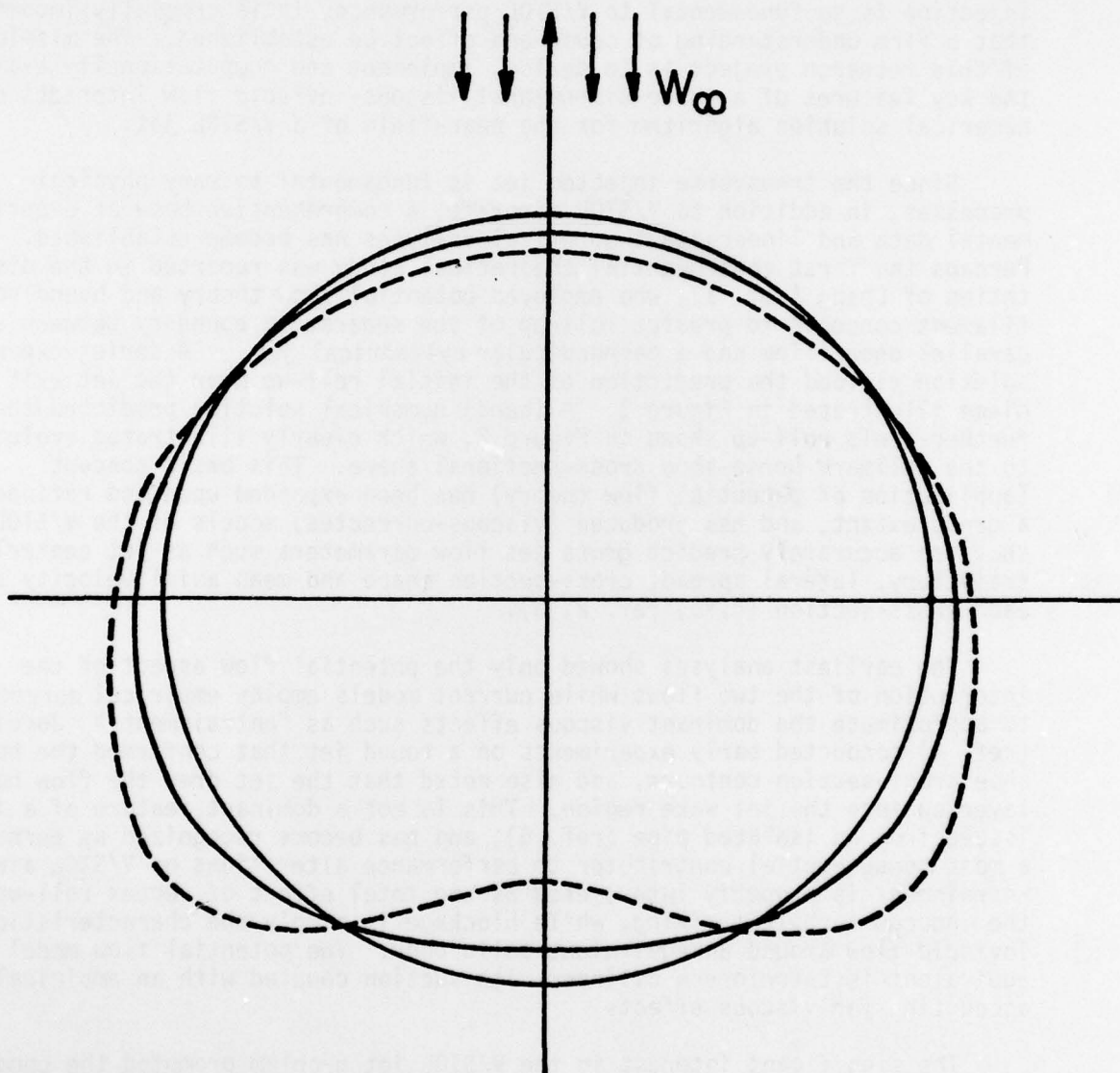
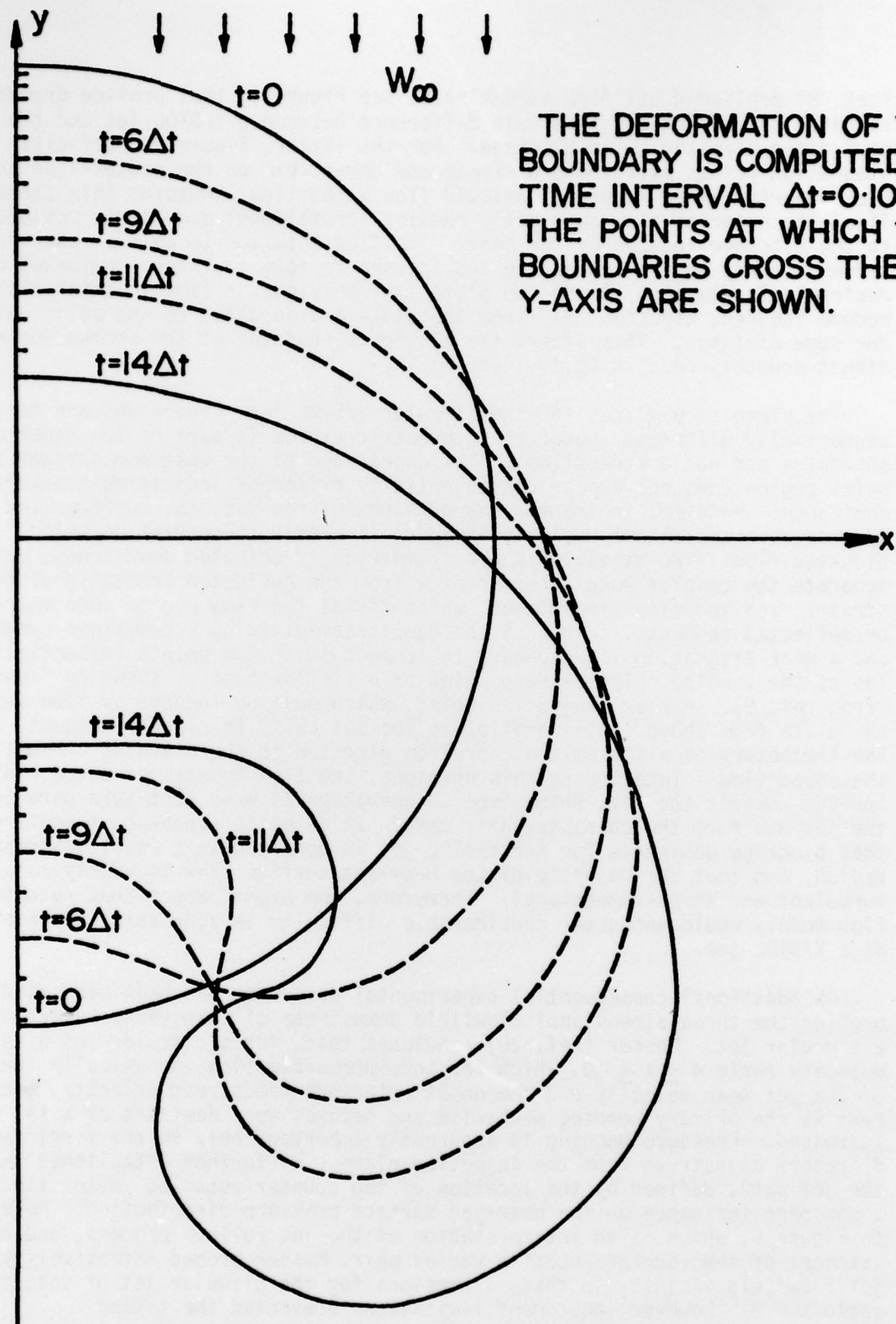Figure 1. Rolling Up Of The Vortex Sheet Near The Jet Exit Plane By
The Crossflow (Ref. 1)

Figure 2.   Rolling Up Of Vortex Sheet By The Crossflow (Numerical Method)
   (Ref. 1)

3

(ref. 8) published oil flow streaklines, see Figure 3, that provide dramatic
evidence of the induced flowfield difference between a V/STOL jet and the
equivalent-diameter solid blockage. For the latter, Figure 3a, definite
stagnation points exist both upstream and downstream on the center-line and
are connected by an apparent inviscid flow streamline. Outside this stream-
line, the exterior flow apparently remains irrotational and simply responds
to the blockage induced by the body. The flow interior to this streamline
curves inwards to the centerline and appears to form a viscous-dominated closed
recirculation region. Since the plate is impervious, a (small) axial flow must
become induced, directed away from the plate and parallel to the solid cylinder
for some distance. Thereafter, the alternate shedding of the Karman vortex
street probably results (c.f., ref. 5).

The plate streamlines for the circular V/STOL jet, Figure 3b, are con-
sequentially different (note: the concentric circle is part of the experimental
apparatus and not a streakline). The appearance of the upstream stagnation
point region does not appear consequentially different indicating blockage-
dominance. However, in the mid-chord region of the jet, the surface flow
becomes directed almost radially inwards, in distinct contrast to solid
blockage flow. Two streamlines are symmetrically oriented downstream, which
separate the complex wake interior flow from the deflected irrotational free-
stream. The incoming streamlines, which divide the flow region into entrained
or deflected segments, intersect the downstream-dividing streamlines symmetrically
and a weak stagnation line appears to connect these two points (essentially on
top of the circle). The close-up view of a similar test is shown in Figure 4
(from ref. 9). A rear stagnation point, which must be induced by flow impinging
the plate from above (anti-parallel to the jet axis) is clearly evident, as is
the trajectory of a streamline therefrom directed to the dividing streamline of
the onset flow. Interior to this envelope, the flow appears directed radially
inwards towards the jet, which from conservation of mass must turn parallel to
the jet and form the characteristic wake. It is quite apparent, therefore,
that blockage dominance for the V/STOL jet is confined to a small upstream
region, and that the majority of the near-jet surface flow is highly rotational,
turbulent and three-dimensional. Therefore, one might expect that potential
flow models would encounter considerable difficulty in addressing the near flow
of a V/STOL jet.

An additional consequential experimental data base has been generated by
probing the three-dimensional flowfield downstream of transverse injection for
a circular jet. Mosher (ref. 10) concludes that, for a circular jet with
velocity ratio $4 \le \lambda \le 10$, which for incompressible flow is basically the ratio
of the jet mean velocity and the onset reference freestream velocity, entrain-
ment is the primary bending mechanism and becomes more dominant as λ is
increased. Pressure bending is apparently important only in the first few jet
diameters downstream from the injection plane. He further established that
the jet path, defined by the location of the counter-rotating vortex flow, was
a dominant influence on the near-jet surface pressure distribution. Referring
to Figure 5, which is an interpretation of the jet roll-up process, and estab-
lishment of the counter-rotating vortex pair, Mosher probed extensively the
jet flowfield vicinity in three-dimensions for the circular jet of velocity
ratio $\lambda = 8$. However, equipment limitations prevented the taking

4
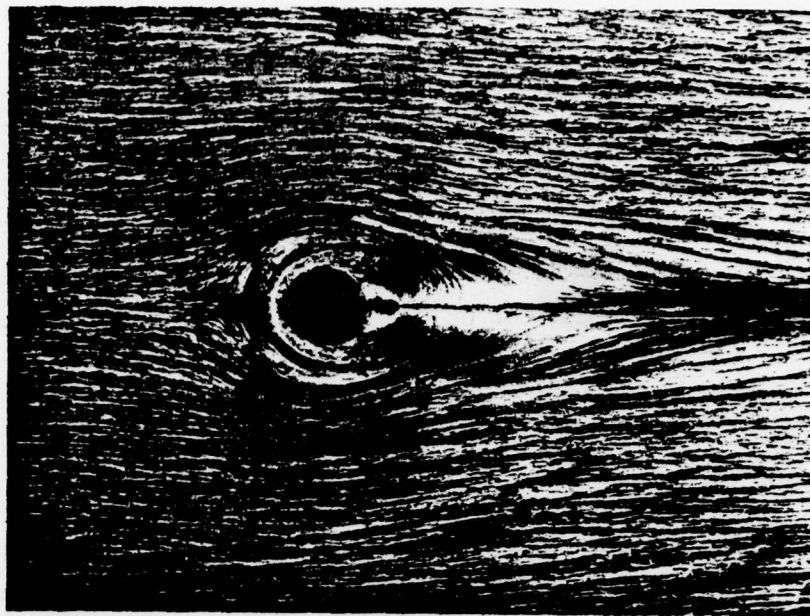
a) Solid Blockage
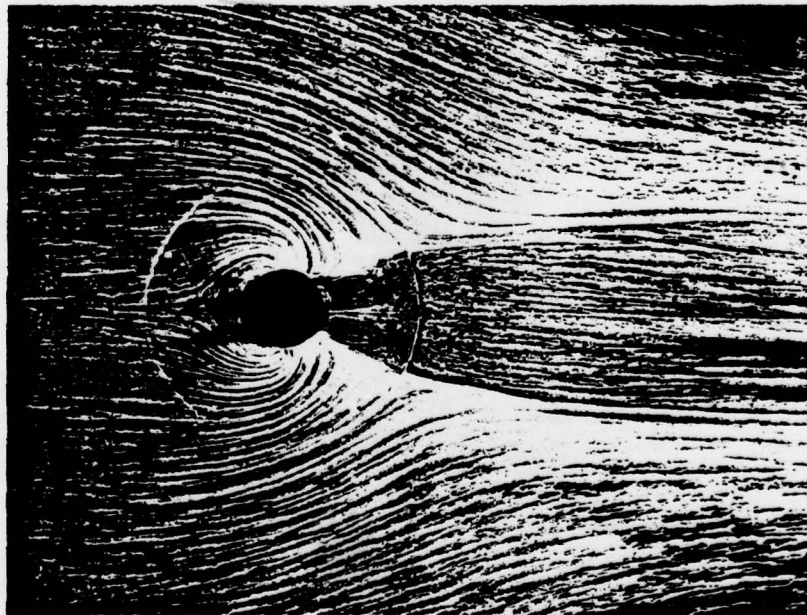
b) Circular Jet at $\lambda = 8$

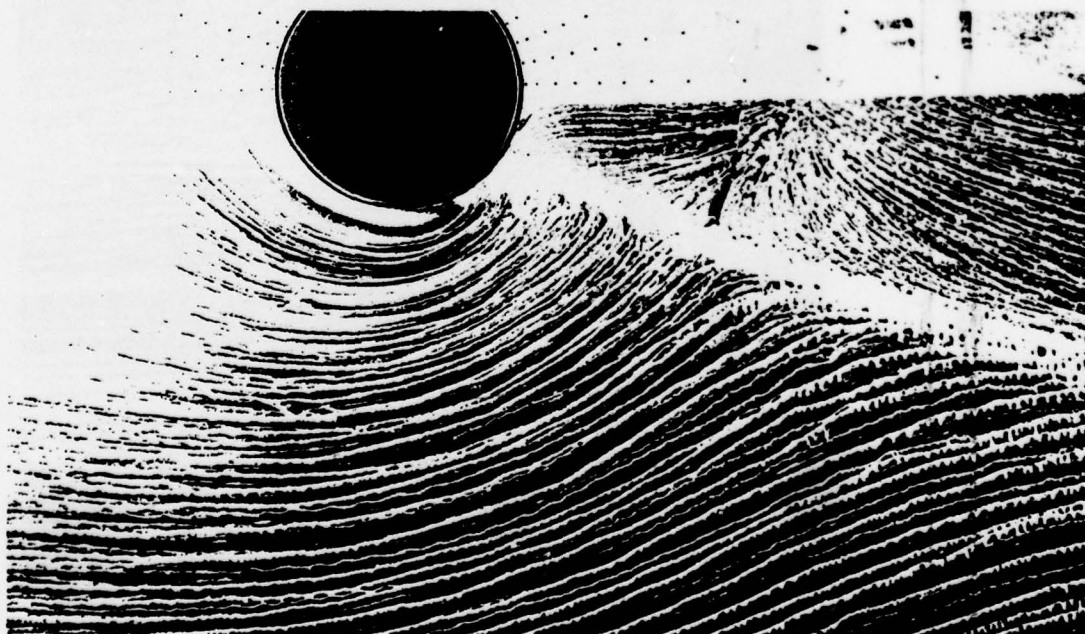Figure 3. Flow Patterns On The Injection Plate (Ref. 8)

5

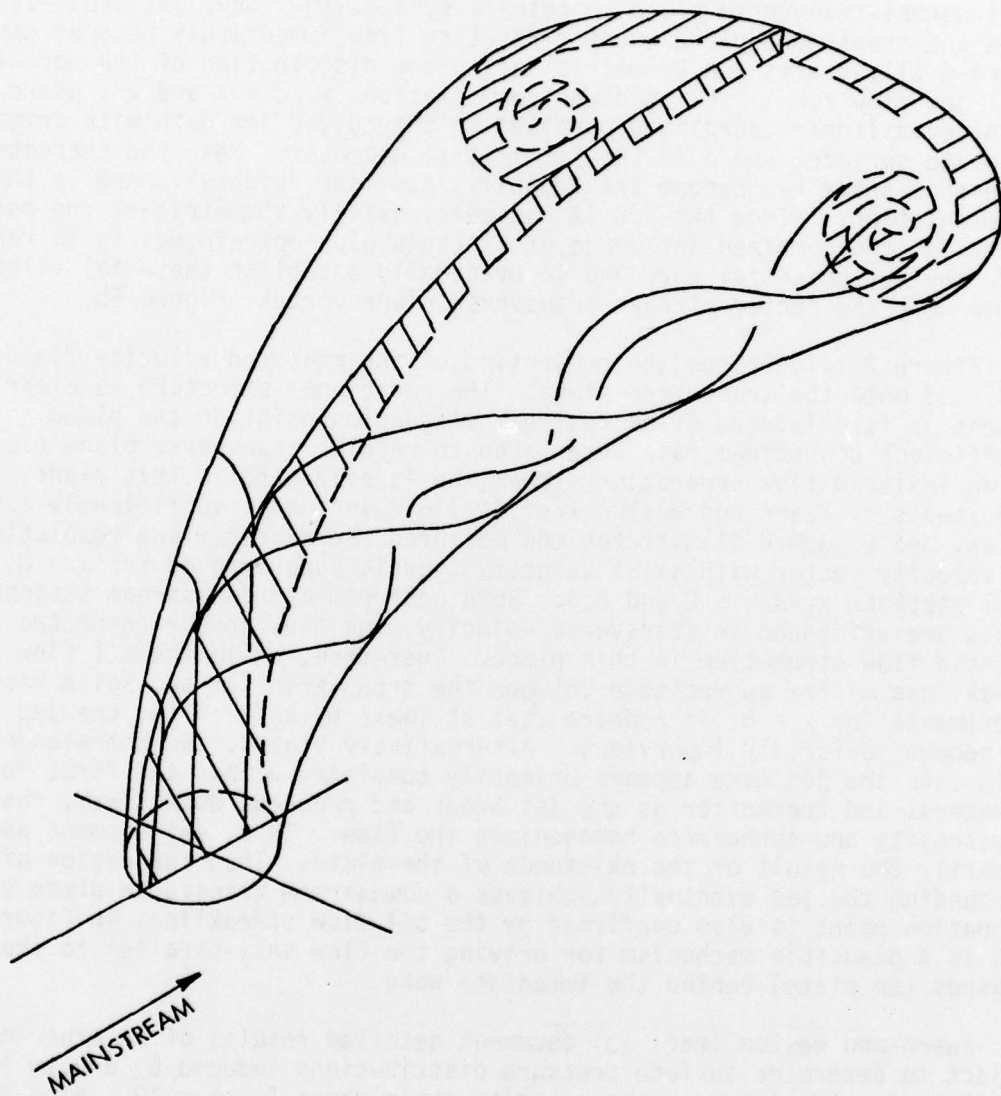Figure 4.   Oil Flow Streaklines For Circular Jet (Ref. 9)

MAINSTREAM

Figure 5. Illustration Of Trailing Vortex Build-Up Behind Circular Jet

of data closer to the plate than about six jet diameters. Kamotani and Greber (ref. 11) also probed the field for $\lambda = 8$ for a circular jet. They pursued considerable data interpretation, in particular determination of the plane orientation along the jet path with unit normal parallel to the local jet dominant axial velocity. Plotting data in vertical planes produced the familiar horse-shoe profiles previously determined by Jordinson. However, when the local velocity vector is resolved into scalar components in the local normal-transverse plane coordinate system, the local jet cross-section shape and transverse plane counter-rotating flow immediately becomes apparent. Figure 6 illustrates the symmetric half-plane distribution of the normal mean axial jet flow for $\lambda = 8$, at downstream stations $x_1/d = 7$ and 23, where x_1 is the curvilinear coordinate parallel to the curved jet path with origin at the plate surface, and d is the jet initial diameter. Note the characteristic horse-shoe shape has become the (equally) familiar "kidney" shape in this representation. Since the jet is basically axially symmetric at the point of injection, the combined influence of blockage plus entrainment is to rapidly erode the jet potential core and to eventually establish the axial velocity maxima near the center of each transverse plane vortex, Figure 6b.

Figure 7 illustrates the projection of the measured velocity field at $x_1/d = 23$ onto the transverse plane. The rotational structure is clearly evident as is existence of an upstream stagnation point in the plane. Insufficient downstream data were taken to resolve transverse plane closure, but an inviscid flow separation streamline is evidenced in this plane. The experiments of Fearn and Weston (ref. 12) did include a sufficiently large region, and Figure 8 illustrates the measured transverse plane resolution of the velocity vector with axial velocity isovels superimposed for $\lambda = 8$, at axial stations $x_1/d = 5.2$ and 8.3. Both upstream and downstream stagnation points are evidenced in transverse velocity, and they appear connected by an inviscid flow streamline in this plane. Therefore, while the oil flow streaklines differ appreciable between the transverse jet and solid blockage experiments for $\lambda = 8$, it appears that at least by $x_1/d \approx 5$, the jet surface has become inviscidly impervious. Alternatively stated, the entrainment of fluid into the jet wake appears primarily completed within the first few jet diameters, and thereafter as the jet bends and proceeds downstream, the action of viscosity and turbulence homogenizes the flow. Thus, entrainment appears primarily the result of the existence of the plate. That the region of flow surrounding the jet eventually achieves a downstream transverse plane velocity stagnation point is also confirmed by the oil flow streaklines in Figures 3-4. This is a plausible mechanism for driving the flow anti-parallel to the jet (towards the plate) behind the immediate wake.

Fearn and Weston (ref. 13) document detailed results of an experimental project to determine surface pressure distributions induced by a 0.1m (4-inch) diameter circular jet over the velocity ratio range $2 < \lambda < 10$. Also included are specific comparisons to O.N.E.R.A. and Mosher data, and the results are presented as detailed C_p distributions on radial rays. Their results show that a region of positive pressure always exists on the upstream side of jet. Large radial pressure gradients are created laterally by the induced mid-side low pressures, and the minimum pressure rotates upstream as λ increases.

8

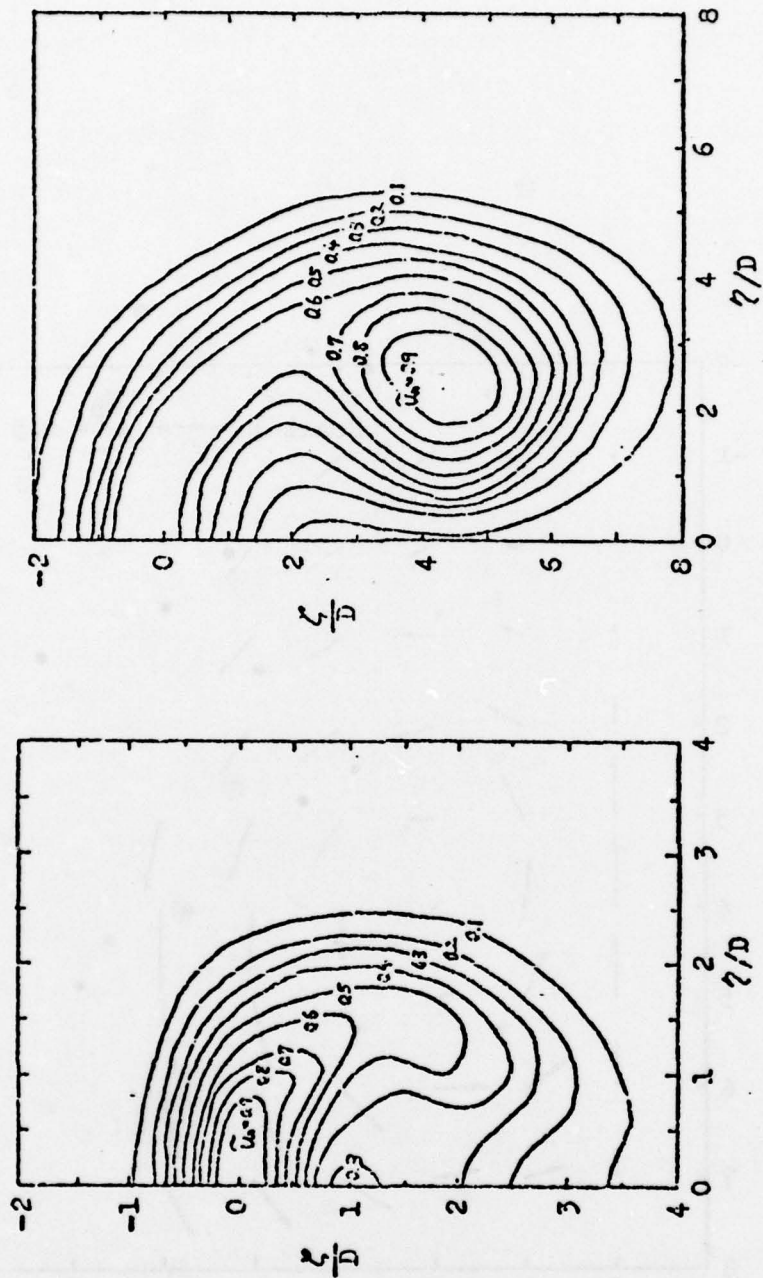Figure 6. Transverse Plane Axial Velocity $\tilde{u}_1$ Contours (Ref. 11)
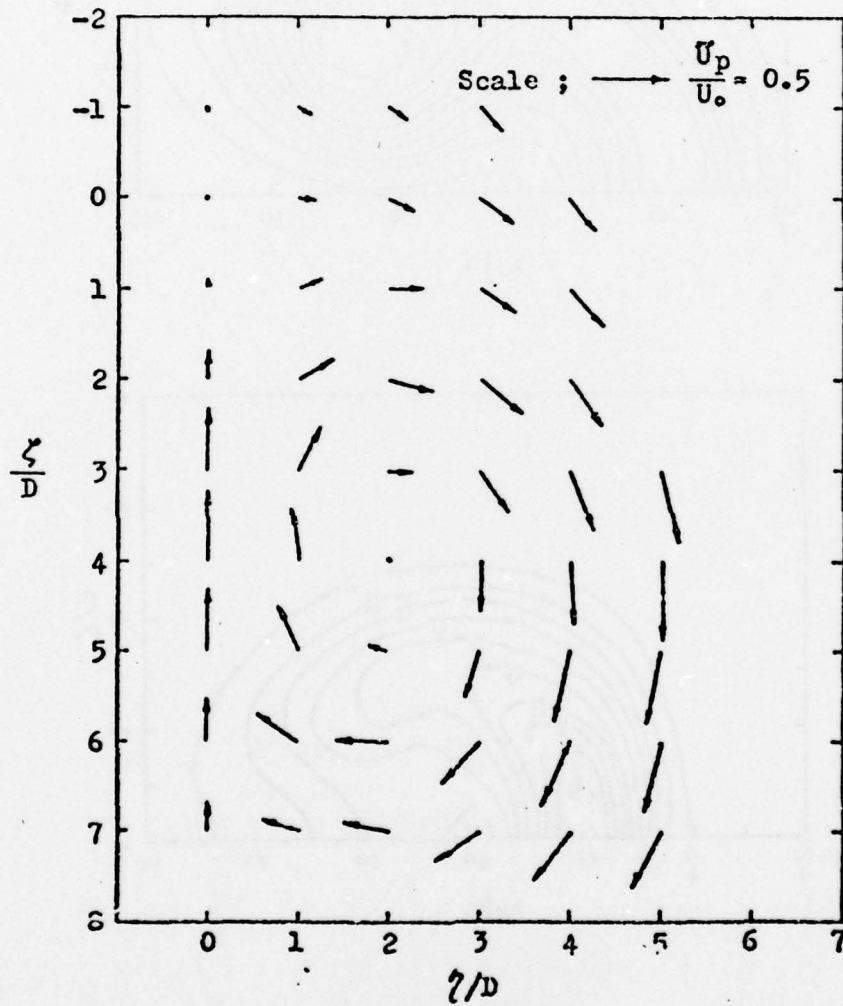
Figure 7. Transverse Plane Velocity $\tilde{u}_\ell$ Vector Plot (Ref. 11) For Circular Jet, $\lambda = 8$, $x_1/d = 23$

- CONTOURS OF CONSTANT U_V/U_ℓ
- U_∞ = 127 FT/SEC
- o JET CENTERLINE

a) $x_1/d = 5.2$, $\lambda = 8$

b) $x_1/d = 8.3$, $\lambda = 8$

Figure 8. Measured Jet Region Velocity $\tilde{u}_j$ Distributions (Ref. 12)

11

The radial pressure gradient along the rearward ray is typically much smaller, and λ appears the controlling parameter.

The conclusions and indications for the round-jet experiments appear to carry over to non-circular jets in essence. Mosher (ref. 10) presents oil flow streaklines for an approximate rectangular cross-section (with rounded corners) with long dimensions both parallel and perpendicular to the onset flow. As expected, the cross-stream orientation produces a relatively larger region of disturbed flow and low surface pressures. Weston and Thames (ref. 14) measured the plate pressure distributions shown in Figure 9 for a rectangular jet of aspect ratio five. It is evident that all cases exhibit large regions of induced negative pressures with extent a function of aspect ratio and orientation. However, it seems fair to conclude that the essential interaction between blockage and entrainment is unchanged by modest jet initial geometry modifications for the velocity ratios evaluated.

These experimental results seem to indicate that the non-potential character of the near jet flow is the dominant determinor of the essential V/STOL jet character. Therefore, it seems rather optimistic to assume that a viscous correction to a potential flow-derived model could adequately describe near-field phenomena without an intractible number of adjustable parameters. This is the base assumption of this analysis as has been con- cluded by others. Specifically, numerical solutions of some form of viscous, rotational flow governing partial differential equations is required. Kotansky and Bower (ref. 15) present a concise summary of the basic dilema in this area which is repeated here as Table 1. A quick scanning of this table, published in 1975, shows that the numerical technology required to predict entrainment and cross-winds is long-term, see columns 5 and 6. The alternative is correlation of results from a large data base which can be quite cumbersome and expensive, see Columns 1-2. Kotansky et. al (ref. 16) presents a solution approach for a full V/STOL aircraft in ground effect using the methodology described in Column 4. A numerical solution procedure applied to considerably simplified forms of the viscous flow Navier-Stokes equations, has also been initiated and belongs to Column 5. Specifically, Bower and Kotansky (ref. 17) report results for an incompressible, two- dimensional planar analysis for a rectangular jet issued from beneath a plane surface into a cross-flow. Extension to a two-equation turbulence model and compressible flow was reported by Bower (ref. 18) and the discussion includes the theoretical extension to three-dimensions using the streamfunction vorticity equation system.

An alternative approach, also belonging to Column 5 of Table 1, is developed herein. The analysis of the experimental data clearly indicates that three-dimensionality is absolutely intrinsic to the flowfield develop- ment; hence, there is no lower dimensional description that can yield meaningful results. The jet and near-field flow is rotational, viscous and undoubtedly highly turbulent. Therefore, for a prediction methodology to be adequate, it must be obtained using some form of the three-dimensional time- averaged Navier-Stokes equations. Furthermore, since the three-dimensional analysis is required, the complete Reynolds stress tensor must be considered

12
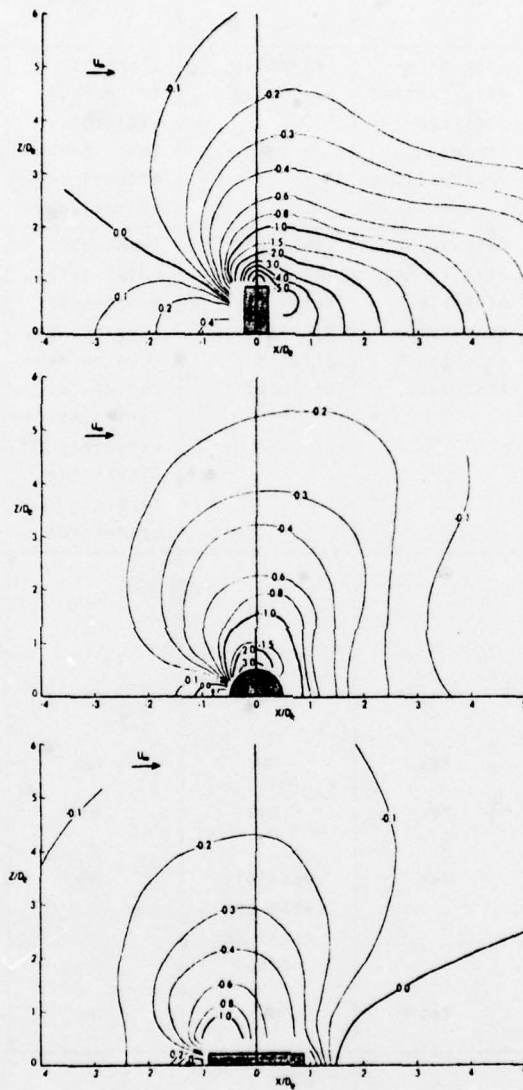
Figure 9. Experimental Contours Of Constant Surface Pressure
Distributions For Various Jets, $\lambda = 4$ (Ref. 14)

13

	① Model and full-scale testing	② Empirical prediction methods based on (1)	③ Potential flow models	④ Patched flow-field models using available regional methods	⑤ Elliptic solution of complete viscous flowfield utilizing turbulence model	⑥ Complete Navier-Stokes solution for high Reynolds number
Major Advantages	Only currently available method for evaluating VTOL configurations	Some parameterization possible through interpolation	Technology available	Elements of technology available. Some viscous effects can be included	Complete mathematical description of physical problem permitting parametric investigation of all pertinent variables	
Major Disadvantages	Inflexible and expensive	Extrapolation usually not possible. Requires voluminous test data	Empirical entrainment data required. No viscous effects included	Techniques complicated, problem-dependent, and require experimental verification. Extremely difficult for complex geometries.	3-5 year development time required	10+ year development time required
(eventual) Capability to predict						
a) Entrainment induced lift loss	Yes	Yes	Yes	Yes	Yes	Yes
b) Fountains	Yes	Yes	No	Yes	Yes	Yes
c) Complex geometries	Yes	Yes	Yes	No	Yes	Yes
d) Cross winds	Yes	Yes	Possibly (with empirical jet data)	No	Yes	Yes
e) Temperature field	Yes	Yes	No	No	Yes	Yes

Table 1.   Prediction of Lift-jet/airframe/ground Interactions (Ref. 15)

14

as applicable. Remote from the plate there is indication of an inviscid flow streamline connecting upstream and downstream, transverse plane velocity stagnation points. Both the initial jet and onset cross-flow velocities are steady and the dominant scalar component of the jet velocity vector is unidirectional, parallel to the curvilinear jet axis.

These observations guided the analysis conducted under this contract which has yielded derivation of a three-dimensional, viscous-inviscid interaction algorithm for detailed prediction of the near-field flow associated with a V/STOL jet injected transverse to a subsonic crossflow. Following establishment of the differential equation systems required solved (in the next section) a complete description of the sequential steps of the iterative interaction algorithm is presented. Table 2 provides a brief summary of the major steps. Following Input, a sequence of inexpensive two-dimensional potential flow solutions are conducted at the injector surface, which yield determination of the interface contour separating the potential and viscous-turbulent solution domains, and the initial distribution of entrainment velocity into the jet region. An interpolation, guided by any available data, yields the required three-dimensional potential flow solution domain shape, Step C. A relatively inexpensive three-dimensional potential solution determines the first estimate of the inviscid pressure distribution on the plate and on the viscous jet region domain boundaries. A modestly inexpensive computational sequence then yields initialization of all dependent variables of the three-dimensional turbulent flow solution, plus distribution of the pressure fields which inter-connect the two solution domains. Step E is a relatively more expensive solution of the complete three-dimensional viscous and turbulent jet flowfield equations. Convergence of the sequence occurs when the potential flow entrainment (which is negative) at the upper extremity of the Step C solution domain and parallel to the jet direction, is in agreement with that predicted by the viscous jet region solution, as affected by entrainment everywhere perpendicular to the jet axis.

Hence, the developed interaction algorithm is based upon existence of entrainment, both as a primary motive force as well as the check on solution compatability. The output of the solution algorithm, Step F, includes the detailed velocity and turbulence correlation distributions within the jet region and the induced pressure distribution on the injector plate. The jet region solution will also yield a computational estimate of the entrained mass flux. The following section develops the interaction algorithm, which requires considerable exposition of differential equation systems. It is hoped the development is adequate without being burdensome. The geometric flexibility of finite element numerical solution methodology is employed to establish the numerics, as well as to generate the computational results discussed in the subsequent section. An Appendix is included to record a more complete development of the viscous and turbulent differential equation systems required for the jet region analysis.

15

Table 2

SUMMARY OF THREE-DIMENSIONAL V/STOL JET INTERACTION ALGORITHM

PHASE	OPERATION	DESCRIPTION
A.	Input	Problem specified by: U_∞ = crossflow velocity $U_j, d_j, \bar{r}_j$ = jet velocity, diameter, axis distribution
B.	2D Potential Flow Computation	1. Find C_p^b for blockage contours on injector plate 2. Extract entrainment velocities at plate.
C.	3D Potential Flow Computation	1. Interpolate interaction surface 2. Distribute entrainment 3. Compute inviscid flow plate C_p
D.	2D Viscous and Turbulent Jet Region Solutions	1. Initialize jet region axial velocity 2. Compute transverse plane velocity distributions 3. Compute turbulence correlation distributions 4. Compute interior pressure distribution
E.	3D Turbulent Jet Region Computation	1. Integrate complete 3D jet region equations using Step D. results for start-up. Yields complete 3D turbulent jet velocity distribution 2. Stop at top of 3D domain of Step C. 3. Compare turbulent jet axial velocity to (negative) entrainment estimated at Step C.2. 4. Repeat analysis starting at Step C.1. if required.
F.	Output	1. Complete 3D turbulent jet region flowfield. 2. C_p distribution on injector plate. 3. Prediction of entrainment volume into jet.

16

Overview

The requirement is to establish a three-dimensional model of the V/STOL jet problem, and the identification of methodology to yield a numerical solution. The only three-dimensional flowfield equation system solvable on present digital computer hardware systems is potential flow. Yet the potential theory-based algorithms, as briefly discussed in the Introduction, have fallen far short of adequately describing the near-jet flowfield, primarily due to lack of an adequate jet-wake model (c.f., ref 19). An alternative model is developed herein that relies on three-dimensional potential theory only to provide pressure boundary conditions for a completely viscous, rotational and turbulent description of the V/STOL jet and the near-region flow. A parabolized form of the steady three-dimensional time-averaged Navier-Stokes equations is derived to describe this jet region flowfield. An algorithm is also developed to couple the two separate differential equation descriptions within an interaction formalism.

Interaction Surface Definition

The viability of an interaction algorithm, for an aerodynamics description, is based solely upon identification of a surface within the flowfield upon which inviscid potential flow boundary conditions can be specified. The classical approach for adding boundary layer effects to an airfoil analysis, for example, has been to assume the inviscid contour corresponds to the *physical thickness everywhere* augmented by the displacement surface δ^* computed by the boundary layer solution. In this case, δ^* is assumed an inviscid streamline, hence impervious to flow.

This appears a valid concept for the V/STOL jet problem only at sufficient distance from the surface of injection. The available data appear to confirm that, for a circular jet at $\lambda = 8$ for example, that this inviscidly-impervious surface develops by about five diameters downstream of injection. Figures 7 and 8 illustrated this observation, the crucial test being existence of an apparent streamline connecting two stagnation points. From Figure 8, the stagnation points exist on the symmetry plane at about +4 jet diameters from the defined center of the jet flow region, and the region extends laterally about the same distance. Hence, for this case at least, the region of viscous dominated rotational flow appears bounded by a nominal circle of radius equal to approximately 4 jet diameters. Experiment (c.f., ref. 11) indicates that the size of this region increases as the jet travels downstream, and that it tends to become nominally elliptical in cross-sectional shape with major axis perpendicular to both the cross-flow velocity vector and the normal to the plate.

17

Adequate vortex models exist to describe this far-field evolution, roll-up, and turning parallel to the cross-flow, see for example reference 12. The present requirement is to describe the flow in the first (say) 4-5 jet diameters downstream of injection. The sole alternative guidance available for definition of an interaction surface is the measured surface C_p and oil streakline photographs. Recalling Figures 3-4 and the pertinent discussion, no inviscid flow streamline is indicated. In particular, mass is specifically injected into the jet wake from the cross-flow. Fortunately, and of specific usefulness here, the interaction surface separating the potential and viscous flow domains need not be an inviscid streamline.

The differential equation governing potential flow is simply the linear Laplacian

$$L(\phi) \equiv \nabla^2\phi = 0 \tag{1}$$

where the dependent variable is the (perturbation) potential function ϕ, defined in terms of the local velocity vector $\vec{u}$, and the reference (cross-flow) velocity $\vec{U}_\infty$ as

$$\vec{u} \equiv \vec{U}_\infty - \nabla\phi \tag{2}$$

Since equation (1) is an illiptic boundary value problem, boundary conditions on ϕ are everywhere required specified. If the boundary corresponds to an inviscid streamline, than $\vec{u}$ must there lie tangential. The equivalent expression is that the dot product of $\vec{u}$ with the normal vector $\hat{n}$ to the surface vanishes, i.e. $\vec{u}.\hat{n} \equiv 0$. From equation (2), the computational equivalent is

$$\nabla\phi.\hat{n} = \vec{U}_\infty.\hat{n} \tag{3}$$

which states teh normal projection of $\nabla\phi$ equals the onset component of U_∞.

Should the boundary surface not be an inviscid streamline, then $\vec{u}.\hat{n}$ does not equal zero but instead equals the inviscid "onset" velocity component $U^\perp$. This is the component of $\vec{u}$, equation (2), that passes through the surface. Therefore, the boundary condition for solution of the potential distribution ϕ becomes

$$\nabla\phi.\hat{n} = \vec{U}_\infty.\hat{n} - u^\perp \tag{4}$$

Use of equation (4), which is simply a modest generalization of equation (3), as the boundary specification for solution of equation (1) for potential flow, yields the required flexability for the V/STOL interaction algorithm. For the streaklines shown in Figure 3a, corresponding to solid blockage, the visible inviscid streamline not surprisingly appears in the nominal shape of an airfoil. Therefore, assume the blockage effect for the V/STOL jet, Figure 3b, is also an airfoil contour, the thickness ratio and chord of which is to be determined. It probably is not totally different from that of the solid blockage contour, but it must be determined. The required data for this is specifically available from the experimental measurements of surface C_p distributions for many configurations.

A planar airfoil contour C_p is readily computed for no "onset" flow, i.e. no entrainment using equations (1)-(3). Since the real flow with entrainment must uniformly involve equal or larger velocities, for any selected airfoil shape, the experimental C_p must be either equal to or more negative than the zero entrainment case. The minimum thickness (ratio) for the no entrainment case is the jet diameter, but no upper-bound exists on the thickness. Therefore, it is reasonable to expect that some blockage contour(s) can be found meeting these requirements. Assuming this valid (as is indeed verified in the next section for the round jet case with $\lambda = 8$), the definition of pressure coefficient C_p yields the local distribution of entrainment velocity $u^\perp$ as

$$C_p = C_p^b - (u^\perp)^2 \tag{5}$$

where C_p^b is the computed blockage-only distribution. The direction of $u^\perp$ is of course inwards; the availability of $\hat{n}$ allows resolution of $u^\perp$ into appropriate scalar components of the local velocity vector $\vec{u}$.

This procedure yields definition of a (range of) inviscid-viscous flow interaction contour(s) on the injection plate surface. The shape of the blockage surface is also known (for the round jet with $\lambda = 8$, at least) at some distance from the plate. Additional experimental data would allow definition of the interaction surface between these extrema. In its absence, it is fair to assume that the surface would smoothly connect the two curves and would have to be determined by the analysis. This requires that an iterative procedure be developed between the potential and viscous flow solutions with interface shape and entrainment the iteration parameters. This leads to derivation of the key feature of pressure coupling within the interaction algorithm.

Pressure Coupling Algorithm

A parabolized form of the steady, three-dimensional time-averaged Navier-Stokes equations will be employed for the jet-wake region flowfield as discussed in the following section. Bearing this in mind, a key element in the parabolization procedure is that the transverse plane pressure distribution and axial pressure gradient be locally solvable as a function for distance along the jet trajectory. This is accomplished by derivation of a differential equation obtained from the divergence of the transverse plane mean flow momentum equations. The detailed development is presented in the Appendix; it is sufficient at this juncture to simply state the derived differential equation. Defining the limited tensor index summation convention, $1 < j < 3$ and $2 \le k, \ell \le 3$, where x_ℓ is the coordinate system spanning the plane transverse to the local jet direction, with unit normal parallel to the x_1 coordinate, the differential equation governing the jet-region pressure distribution is

$$L(\bar{p}) = \frac{\partial}{\partial x_\ell} \left[\frac{\partial \bar{p}}{\partial x_\ell} + \frac{\partial}{\partial x_j} (\bar{\rho}\tilde{u}_j\tilde{u}_\ell) - \frac{\partial}{\partial x_k} (\bar{\sigma}_{\ell k} - \overline{\rho u_\ell' u_k'}) \right] = 0 \qquad (6)$$

The overbar and over-tilde in equation (6) signify time-averaged and mass-weight time-average respectively, and $\bar{p}$ is pressure, $\bar{\rho}$ is density, $\tilde{u}_j$ is velocity vector, $\bar{\sigma}_{\ell k}$ is the Stokes viscous stress tensor, and $\overline{\rho u_\ell' u_k'}$
is the Reynolds stress tensor.

The solution algorithm for equation (6) is based upon the observation that the solution of a linear, elliptic Poisson equation consists of a complementary and a particular contribution as

$$\bar{p}(x_i) = p_c(x_i) + p_p(x_i) \qquad (7)$$

By definition, the complementary solution satisfies the homogeneous form of equation (7), i.e.,

$$L(p_c) = \frac{\partial^2 p_c}{\partial x_\ell^2} = 0 \qquad (8)$$

subject to the known boundary conditions for pressure $\bar{p}(x_i)$. Since the interface inviscid flow pressure distribution is everywhere known,

$$\bar{p}(\bar{x}_\ell) = p^I(\bar{x}_\ell) = p_c(\bar{x}_\ell) \qquad (9)$$

20

In equation (9), $\bar{x}_\ell$ indicates x_ℓ constrained to the interfacial boundary of the viscous solution domain, and pI is the (inviscid flow) pressure level distribution. Elsewhere, on the jet region central symmetry plane specifically, the appropriate boundary condition is vanishing normal gradient,

$$\ell(p_c) = \frac{\partial}{\partial x_\ell} \, p_c \cdot \hat{n}_\ell = 0 \qquad (10)$$

Therefore, the solution to equations (8)-(10) provides determination of the pressure distribution interior to the viscous jet region induced by the impressed cross-flow velocity (distribution). Since, as presented in the previous section, the inviscid flow pressure distribution is a priori known, the solution to equation (8) provides the required pressure coupling of the interaction algorithm.

The particular pressure distribution p_p modifies the computed complementary pressure distribution to account for viscous modifications within the jet region. The particular solution p_p is any function satisfying equation (6) with homogeneous boundary conditions on interface segments coincident with p^I known. Since the convection term in equation (6) vanishes identically on a symmetry plane, the appropriate form of the boundary condition is

$$\ell(p_p) = \frac{\partial p}{\partial x_\ell} \hat{n}_\ell - \frac{\partial}{\partial x_k} \left[\bar{\sigma}_{\ell k} - \overline{\rho u_k' u_\ell'} \right] \hat{n}_\ell = 0 \qquad (11)$$

Since the second term in equation (11) obliterates the boundary condition stress term in equation (6), the appropriate Poisson equation for p_p must be the inviscid form.

$$L(p_p) = \frac{\partial}{\partial x_\ell} \left[\frac{\partial p_p}{\partial x_\ell} + \frac{\partial}{\partial x_j} \left(\bar{\rho} \tilde{u}_j \tilde{u}_\ell + \overline{\rho u_\ell' u_k'} \right) \right] = 0 \qquad (12)$$

Equations (6)-(12) define the algorithm for determination of pressure distributions in the three-dimensional parabolic viscous flow solution. The pressure solutions are summed, as in the defining equation (7) and differentiated to form the transverse pressure gradient field. This completes definition of the pressure coupling algorithm for the interaction algorithm, and attention is now focused on establishment of the viscous jet region differential equation description.

21

Jet Region Governing Differential Equation System

The singular requirement for the proposed viscous-invisid interaction algorithm and a significant contribution of this study is derivation and development of a numerically tractible differential equation system describing the three-dimensional viscous and turbulent flowfield within the jet region interior to the interaction interface. The developed differential equation system is named the three-dimensional parabolic Navier-Stokes (3DPNS) equations, and has emerged after several years development in a consequentially complete form. The 3DPNS system is obtained from the complete, non-linear time-averaged Navier-Stokes partial differential equation set, following application of simplifying assumptions which are:

(1) The flowfield is steady

(2) A dominant direction for the mean flow is uniformly discernible

(3) In this direction (only) diffusion is negligible compared to all other processes including convection, and

(4) The overall three-dimensional elliptic boundary value character is enforced by interaction with a concomitantly computed potential flow

The examiniation of the character of the V/STOL jet-region flow, as discussed to the present, indicates that each of these assumptions is satisfied. The flowfield can be assumed steady, and because of existence of the plate of injection, the jet and jet-wake flows are uniformly directed therefrom along the jet axis. (The sole exception appears to occur at the rear stagnation region, as evidenced in the oil streakline photos, see Figure 3b and 4. The jet-region solution domain therefore can at most intersect this location, but cannot include it. This places a limitation on the analysis that can be removed only by going to a complete three-dimensional Navier-Stokes description which is computationally intractible at present.) For sufficiently large jet velocity ratio λ, the third assumption appears valid, and the entire development is derived within an interaction algorithm with inviscid exterior three-dimensional flowfield.

Establishement of the 3DPNS differential equation system is a fairly consuming process and the derivation is presented in completeness by Baker (ref. 20). The Appendix of this report presents a summary of the developmental procedures. For the purpose of completing the interaction solution algorithm definition, the 3DPNS differential equation system that governs convection, diffusion, generation and annihilation of both mean flow and turbulence correlation phenomena within the jet-wake solution domain lying interior to the interaction surface, is

22

$$L(\bar{\rho}) \;\; = \frac{\partial}{\partial x_i} (\bar{\rho}\tilde{u}_i) = 0 \tag{13}$$

$$L(\bar{\rho}\tilde{u}_1) = \frac{\partial}{\partial x_i} (\bar{\rho}\tilde{u}_i\tilde{u}_1) + \frac{\partial \bar{p}}{\partial x_1} - \frac{\partial}{\partial x_\ell}\left[\frac{\bar{\mu}}{Re}\frac{\partial \tilde{u}_1}{\partial x_\ell} - \overline{\rho u_1' u_\ell'}\right] = 0 \tag{14}$$

$$L(\overline{\bar{\rho}\tilde{u}_2}) = \frac{\partial}{\partial x_i} (\bar{\rho}\tilde{u}_i\tilde{u}_2) + \frac{\partial \bar{p}}{\partial x_2} - \frac{\partial}{\partial x_\ell}\left[\frac{\bar{\mu}}{Re}\left(\frac{\partial \tilde{u}_2}{\partial x_\ell} + \frac{\partial \tilde{u}_\ell}{\partial x_2}\right) - \overline{\rho u_2' u_\ell'}\right] = 0 \tag{15}$$

$$L(\bar{\rho}\tilde{u}_3) = \frac{\partial}{\partial x_i} (\bar{\rho}\tilde{u}_i\tilde{u}_3) + \frac{\partial \bar{p}}{\partial x_3} - \frac{\partial}{\partial x_\ell}\left[\frac{\bar{\mu}}{Re}\left(\frac{\partial \tilde{u}_3}{\partial x_\ell} + \frac{\partial \tilde{u}_\ell}{\partial x_3}\right) - \overline{\rho u_3' u_\ell'}\right] = 0 \tag{16}$$

$$L(k) \;\; = \frac{\partial}{\partial x_i} (\bar{\rho}\tilde{u}_i k) - \frac{\partial}{\partial x_i}\left[\bar{\rho}\left(\frac{\bar{\nu}}{Re} + C_k \frac{k}{\epsilon}\overline{u_i' u_k'}\right)\frac{\partial k}{\partial x_k}\right] + \overline{\rho u_i' u_k'}\frac{\partial \tilde{u}_k}{\partial x_i} + \bar{\rho}\epsilon = 0 \tag{17}$$

$$L(\epsilon) \;\; = \frac{\partial}{\partial x_i} (\bar{\rho}\tilde{u}_i\epsilon) - \frac{\partial}{\partial x_i}\left[\bar{\rho}\left(0 + C_\epsilon \overline{u_i' u_k'}\frac{k}{\epsilon}\right)\frac{\partial \epsilon}{\partial x_k}\right]$$

$$+ C_\epsilon^1 \overline{\rho u_i' u_\ell'}\frac{\epsilon}{k}\frac{\partial \tilde{u}_k}{\partial x_n} + C_\epsilon^2 \bar{\rho}\epsilon^2 k^{-1} = 0 \tag{18}$$

Recall the index limited summation convention, $1 \leq i \leq 3$ and $2 \leq k, \ell \leq 3$, and that the variables appearing in equations (13)-(18) are the mass-weighted, time-averaged density, pressure and velocity and dynamic Reynolds stress tensor. Re is the reference Reynolds number. Equations (17)-(18) are the three-dimensional parabolic form of the transport equations for turbulence kinetic energy k and isotropic dissipation function ϵ, defined as

$$k \;\; \equiv \;\; \frac{1}{2} \overline{u_i' u_i'} \tag{19}$$

$$\frac{2}{3}\delta_{ij}\epsilon \;\; \equiv \;\; 2\bar{\nu}\overline{\frac{\partial u_i'}{\partial x_k}\frac{\partial u_j'}{\partial x_k}} \tag{20}$$

These equations are required solved, in concert with equations (13)-(16), to complete closure of the 3DPNS system for the Reynolds stress distribution. The dynamic Reynolds stress is assumed the product of the time-averaged density and the kinematic Reynolds stress tensor, the parabolic components of which in principal coordinates are (ref. 21)

23

$$\overline{u_1'u_1'} = C_1 k$$

$$\overline{u_2'u_2'} \equiv C_3 k - 2C_4 \frac{k^2}{\varepsilon} \frac{\partial \tilde{u}_2}{\partial x_2} \qquad\qquad - C_2 \frac{k}{\varepsilon} C_4 \frac{k^2}{\varepsilon} \left(\frac{\partial \tilde{u}_1}{\partial x_2}\right)^2$$

$$\overline{u_3'u_3'} = C_3 k - 2C_4 \frac{k^2}{\varepsilon} \frac{\partial \tilde{u}_3}{\partial x_3} \qquad\qquad - C_2 \frac{k}{\varepsilon} C_4 \frac{k^2}{\varepsilon} \left(\frac{\partial \tilde{u}_1}{\partial x_3}\right)^2$$

$$\overline{u_1'u_2'} = \qquad - C_4 \frac{k^2}{\varepsilon} \frac{\partial \tilde{u}_1}{\partial x_2}$$

$$\overline{u_1'u_3'} = \qquad - C_4 \frac{k^2}{\varepsilon} \frac{\partial \tilde{u}_1}{\partial x_3}$$

$$\overline{u_2'u_3'} = \qquad - C_4 \frac{k^2}{\varepsilon} \left[\frac{\partial \tilde{u}_2}{\partial x_3} + \frac{\partial \tilde{u}_3}{\partial x_2}\right] - C_2 \frac{k}{\varepsilon} C_4 \frac{k^2}{\varepsilon} \frac{\partial \tilde{u}_1}{\partial x_2} \frac{\partial \tilde{u}_1}{\partial x_3} \qquad (21.)$$

Finally, the various C_i and C_q^α are correlation constants of the turbulent closure model, see the Appendix.

Equations (14)-(18) are five initial-value, two-dimensional elliptic boundary value, non-linear partial differential equations written on the dependent variables of jet region velocity $\tilde{u}_j$ and turbulence correlations k and ε. Equation (13) is a constraint equation enforcing conservation of mass, which is inserted directly into the right-hand non-homogeniety of the particular pressure Poisson equation (12). The axial pressure gradient distribution $\partial \bar{p}/\partial x_1$, used to drive the dominant jet-flow momentum equation (14), is established solely from the complementary pressure solution. The total computational pressure field is employed to drive the transverse plane velocity components, equations (15)-(16).

The solution domain for equations (14)-(18) is the three-dimensional region interior to the interface surface and closed from below by the injection plate, see Figure 10. The domain is open-ended in the downstream jet direction, the result of the parabolizing simplification. Hence, the 3DPNS system is initial-value on the x_1 curvilinear coordinate, Figure 10, and the solution is started at or near the injection plate surface. As a consequence, initial-condition distributions are required specified for all dependent variables $\{q\} \equiv \{\bar{p}, \tilde{u}_j, k, \varepsilon\}$ at this location. This in itself is a consequential computational problem since in reality all that is known is the (nominal) jet velocity U_1, on a circle of diameter d, and the distribution of the tangential and entrainment velocity components of $\tilde{u}_\ell$ on the interface surface. Procedures have been developed to meet the differential equation requirements, however, and are discussed with the numerical results. Boundary conditions are required specified everywhere on the (two-dimensional) interface surface to render equations (14)-(18) a well-posed problem description.

24

At the solution initiation plane, and as a consequence of the iterative inter-action algorithm, the distribution of the tangential and entrainment components of the transverse plane velocity field $\tilde{u}_\ell$ are everywhere known from the exterior potential flow C_p distribution. The boundary conditions for $\tilde{u}_1$ can be similarly extracted from the exterior potential solution since a non-zero axial (x_1) pressure gradient induces a corresponding parallel velocity component. The boundary conditions for k and ε are specified either to agree with the freestream turbulence level, if known, or as a vanishing normal deriv-ative. Although the theory is conceptually extendible to compressible and/or heated, dissimilar jets, the current analysis is restricted to constant uniform density flows.

Coordinate System Descriptions

Experimental evidence confirms that the cross-sectional area and shape of the V/STOL jet interaction surface is strongly a function of distance along the jet path. For the circular jet at $\lambda \approx 8$, for example, the cross-section changes from an approximate 35% thick airfoil at the injection surface to almost circular at $x_1/d = 5.3$. A requirement of the 3DPNS analysis of the jet-region flow evolution, therefore, is to match a generally non-regular shaped solution domain closure that changes with solution progression down-stream. Furthermore, since x_1 is a curve, the entire problem must be cast in an appropriate curvilinear coordinate system.

The overall requirements are met by employing a finite element-based numerical solution algorithm for solving the 3DPNS equations. Even with this inherent geometric flexibility, a grid stretching coordinate transformation is required employed such that the transverse plane discretization continuously spans the entire interior bounded by the interaction surface. Figure 10 illustrates the global x, y, z coordinate system, with origin at the initial jet center, and the curvilinear x_i system. The x_1 coordinate is defined as everywhere parallel to the jet centerline, defined as the locus of extremum $\tilde{u}_1$ lying on the symmetry centerplane (c.f., ref. 12). For simplicity of illustration, assume that the jet region interface surface is required to stretch only in the lateral direction, i.e. parallel to x_2. A coordinate stretching transformation that will continuously place the lateral span between the jet symmetry plane and the interface surface onto a constant length is

$$\eta \equiv \frac{x_2 - f_1(x_1)}{\left[f_2(x_1) - f_1(x_1)\right]f^{-1}} \tag{22}$$

In equation (22), $f_1(x_1)$ is the symmetry plane, $f_2(x_1)$ is the maximum lateral span of the interface surface as a function of location x_1, and f is a nor-malizing factor. The chain rule for differentiation yields

$$\frac{\partial}{\partial x_1} = \frac{\partial}{\partial \xi}\frac{d\xi}{dx_1} + \frac{\partial}{\partial \eta}\frac{d\eta}{dx_1} = \frac{\partial}{\partial \xi} - \left[\frac{f_1'}{(f_2 - f_1)/f} + \frac{f_1'}{f_2 - f_1}\right]\frac{\partial}{\partial \eta} \tag{23}$$
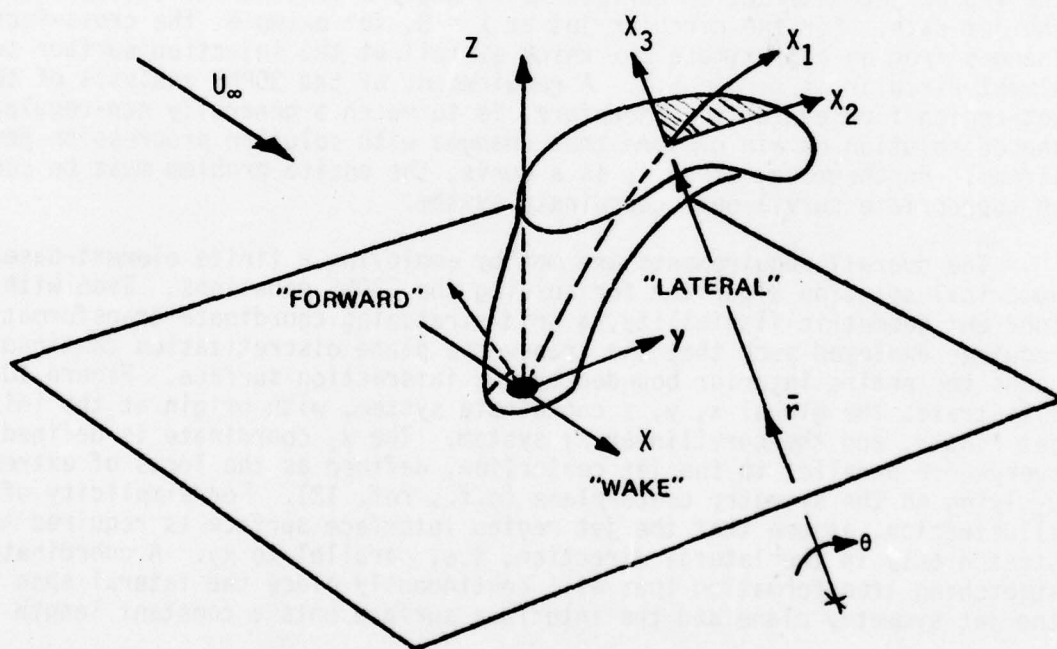
Figure 10. Coordinate Systems For Interaction Algorithm

where superscript prime denotes the ordinary derivative with respect to x_1. Hence, in terms of coefficients h_i, $1 \leq i \leq 3$,

$$h_i \equiv \begin{Bmatrix} f(f_2 - f_1)^{-1} \\ f_1' h_1 \\ f^{-1}(f_2' - f_1') h_1 \end{Bmatrix} \tag{24}$$

related to the metric of equation (22), the spatial derivatives in 3DPNS are reexpressed as

$$\frac{\partial}{\partial x_1} = \frac{\partial}{\partial \xi} - \left[h_2 + \eta h_3 \right] \frac{\partial}{\partial \eta}$$

$$\frac{\partial}{\partial x_2} = h_1 \frac{\partial}{\partial \eta} \tag{25}$$

Then computations would be performed in the fixed ξ, η, x_3 coordinate system.

In general, the interface surface will expand in both the x_2 and x_3 coordinate directions as the jet proceeds downstream. The required generalization of equation (22) is

$$\{n_i\} \equiv \begin{Bmatrix} x_1 \\[2mm] \dfrac{x_2 - f_{21}(x_1)}{[f_{22}(x_1) - f_{21}(x_1)]/f_2} \\[4mm] \dfrac{x_3 - f_{31}(x_1)}{[f_{32}(x_1) - f_{31}(x_1)]/f_3} \end{Bmatrix} \tag{26}$$

In equation (26), f_{2i} are the counterparts of f_i in the one-dimensional case while f_{3i} describe the extremum span of the interface surface parallel to the x_3 coordinate direction. Again employing the chain rule for differentiation on x_i yields

27

$$\frac{\partial}{\partial x_1} = \frac{\partial}{\partial \eta_1} - \left[h_{22} + \eta_2 h_{23} \right] \frac{\partial}{\partial \eta_2} - \left[h_{32} + \eta_3 h_{33} \right] \frac{\partial}{\partial \eta_3}$$

$$\frac{\partial}{\partial x_2} = h_{21} \frac{\partial}{\partial \eta_2}$$

$$\frac{\partial}{\partial x_3} = h_{31} \frac{\partial}{\partial \eta_3} \tag{27}$$

The functions $h_{\ell i}$, $1 \leq i \leq 3$, are again related to the metric of the coordinate transformation, equation (26), and are defined as

$$\{h_{\ell i}\} \equiv \begin{Bmatrix} f_\ell (f_{\ell 2} - f_{\ell 1})^{-1} \\ h_{\ell 1} f'_{\ell 1} \\ h_{\ell 1} f_\ell^{-1} (f'_{\ell 2} - f'_{\ell 1}) \end{Bmatrix} \tag{28}$$

The superscript prime denotes the ordinary derivative with respect to x_1. The η_i coordinate system is fixed in the transform space and hence insensitive to x_1.

One additional transformation is required to account for x_1 being curvilinear. Since in the computational solution, integration of the 3DPNS equations occurs step-by-step, displacements parallel to the x_1 coordinate are re-expressed in terms of an angular displacement θ as

$$dx_1 = \bar{r}(x_1) d\theta \tag{29}$$

In equation (29), $\bar{r}$ is the local radius to the jet centerline, and θ is measured from the negative x axis of the global coordinate system, see Figure 10. Ample experimental data are available to evaluate $\bar{r}(x_1)$ for circular, square and rectangular V/STOL jets over a range of velocity ratios. For example, Figure 11a illustrates the curves determined by McMahon and Mosher (ref. 6) for circular and rounded-corner rectangular jets. Figure 11b, from reference 12, illustrates the collapse of circular jet data onto a universal curve obtained using the jet velocity ratio as a similarity parameter. Kamotani and Greber (ref. 11) determined that, using their data for the circular jet for $4 \leq \lambda \leq 10$, the equation of the jet centerline for all cases was expressible as

28
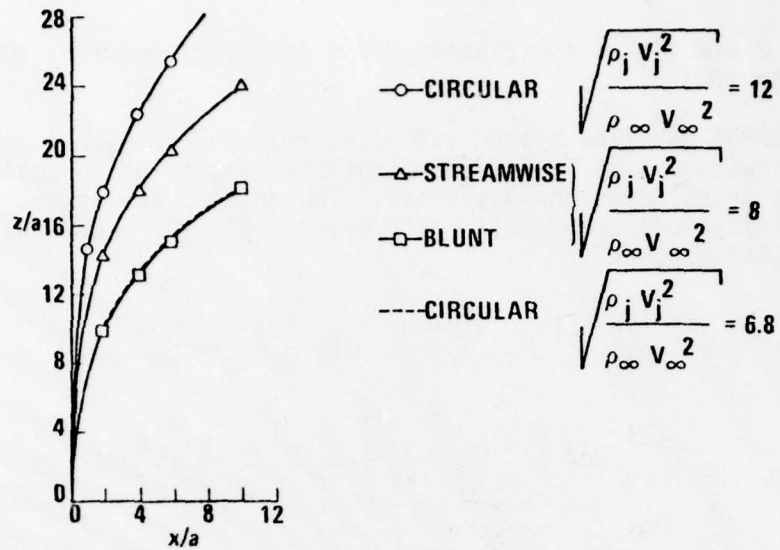
a) Various Jet Shapes (Ref. 6)
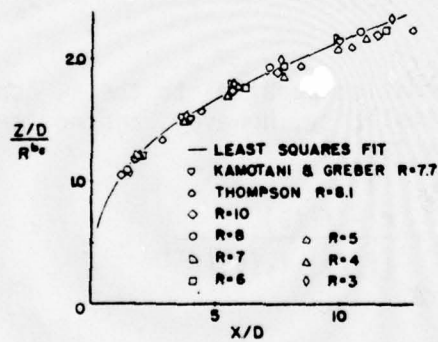
b) Circular Jet at Various λ (Ref. 12)

Figure 11. Measured Jet Centerline Trajectories

29

$$\frac{z}{\frac{1}{2}d}\left[\frac{U_\infty}{U_j}\right]^{0.94} = 0.623\left[\frac{x}{\frac{1}{2}d}\right]^{0.445} + 0.290 \tag{30}$$

The x and z are global coordinates and d is the diameter of the jet orifice in equation (30)

The 3DPNS equation system (13)-(18) must be expanded into the $x_i \equiv \{x_1, x_2, x_3\} \equiv \{\theta, z, r\}$ coordinate system, prior to employing the grid stretching transformations described. The details are messy, but the end point modifications are modest. For example, the x_1 (dominant flow) momentum equation (14) becomes

$$L(\tilde{u}_\theta) = \frac{1}{r}\bar{\rho}\tilde{u}_\theta\frac{\partial\tilde{u}_\theta}{\partial\theta} + \bar{\rho}\tilde{u}_r\frac{\partial\tilde{u}_\theta}{\partial r} + \bar{\rho}\tilde{u}_z\frac{\partial\tilde{u}_\theta}{\partial z} + \frac{1}{r}\bar{\rho}\tilde{u}_r\tilde{u}_\theta$$

$$+ \frac{1}{r}\frac{\partial p_c}{\partial\theta} - \frac{\partial}{\partial r}\left[\frac{\partial\tau_{r\theta}}{\partial r}\right] - \frac{\partial}{\partial z}\left[\frac{\partial\tau_{3\theta}}{\partial z}\right] = 0 \tag{31}$$

There is an added convection term and the total stress tensor $\tau_{k\ell}$ has the scalar components in $\{\theta, z, r\}$.

$$\tau_{r\theta} \equiv \bar{\rho}\nu^e\left[\frac{1}{r}\frac{\partial\tilde{u}_r}{\partial\theta} + r\frac{\partial}{\partial r}\left[\frac{\tilde{u}_\theta}{r}\right]\right]$$

$$\tau_{z\theta} \equiv \bar{\rho}\nu^e\left[\frac{\partial\tilde{u}_\theta}{\partial z} + \frac{1}{r}\frac{\partial\tilde{u}_z}{\partial\theta}\right] \tag{32}$$

The grid stretching transformation parallel to the x_2 coordinate is unaffected. Viewing equation (22) for simplicity, however, and noting that $x_3 = r$ in the present case, the transformation is

$$r' = \frac{r - f_1(\theta)}{\left[f_2(\theta)-f_1(\theta)\right]f^{-1}} \tag{33}$$

The $f_i(\theta)$ describe the transverse extent of the interface surface parallel to the r axis and are assumed expressed as

$$f_i(\theta) = \bar{r}(1 + a_i\theta) \tag{34}$$

Here, $\bar{r}$ is the radius of the circle with chord coincident with the local tangent to x_1 and a_i is the required stretching parameter. Proceeding through the steps, as discussed, and noting that the required x_1 derivative always appears as $r^{-1}\partial/\partial\theta$, the polar coordinate system equivalent of equations (25) becomes

$$\frac{\partial}{\partial x_1} \rightarrow \frac{1}{r}\frac{\partial}{\partial\theta} = \frac{1}{r}\frac{\partial}{\partial\theta'} - \left[h_2 + r'h_3\right]\frac{\partial}{\partial r'}$$

$$\frac{\partial}{\partial x_2} \rightarrow \frac{\partial}{\partial r} = h_1\frac{\partial}{\partial r'} \tag{35}$$

The h_i defined in equation (35) are identical to those in equation (24) but divided by $\bar{r}$. In actual practice the inverse r modifying $\partial/\partial\theta'$ can be replaced by the constant $\bar{r}$ for sufficiently large $\bar{r}$, as occurs in the near-field jet region, for example.

Interaction Solution Algorithm

The exterior potential flow and interior 3DPNS differential equation systems, required solved for the V/STOL jet interaction algorithm, have been identified. The boundary separating these two solution domains is the inter-action surface upon which computed flowfield variables must come into agreement. The geometry of the intersection of the interaction surface with the injection plate is assumed known, as determined by comparison of blockage plus entrainment pressure predictions with experimental data. The radii of the family of circles locally tangent to the jet trajectory is also known from experimental data. In many instances, for example, the circular jet at $\lambda = 8$, the geometry of the intersection of the interaction surface with the trans-verse plane, perpendicular to the jet axis, is also known at one or more down-stream stations. The interaction surface geometry between the injection plate and downstream intersections is typically unknown.

Even if the interaction surface description were everywhere known, an iteration procedure is required developed between the 3DPNS and 3Dϕ solutions. The basic iteration parameter for assessment of convergence is the accelera-tion (parallel to the jet axis) of the fluid contained within and entrained into the 3DPNS solution domain. Figure 12 illustrates the symmetric half-domain employed for the 3Dϕ solutions discussed in the next section. The 3Dϕ solution requires the onset velocity be everywhere specified on the domain boundary, recall equations (1)-(4). This includes the top or "lid" of the domain, shown as a plane parallel to the global x, y plane. The loss of mass
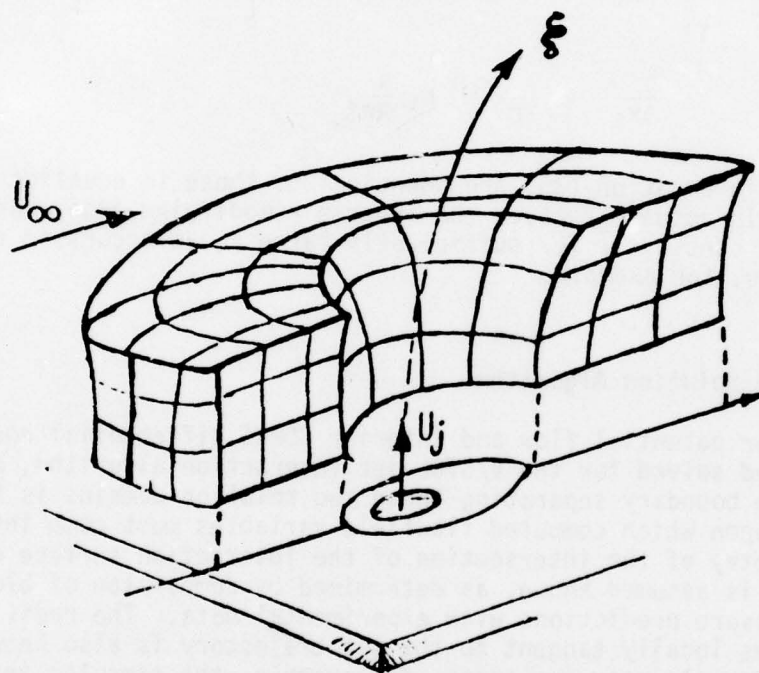
31

Figure 12. Three-Dimensional Potential Flow Solution Domain

to the 3DPNS solution domain is termed the entrainment $u^{\perp}$. As a consequence, an acceleration of $\bar{u}_1$ is distributed throughtout the 3DPNS interior by the action of continuity, equation (13). Hence, the 3DPNS solution will yield $\bar{u}_1 > 0$ selectively at the 3Dϕ "lid" intersection with the 3DPNS domain, see Figure 12. This results in a non-zero "onset" velocity boundary condition for 3Dϕ, which can be distributed across the lid by interpolation to zero at the lateral extremity.

Hence, the action of entrainment from the 3Dϕ solution into the 3DPNS solution becomes reflected as an onset velocity boundary condition modification for 3Dϕ. The two solutions are accepted when this difference in onset velocity components vanishes to within a specified tolerance. Since the elevation of the 3Dϕ lid above the plate is not required to be farfield, the interaction solution iteration is presumably operable on progressively larger domains as generated by addition of layers to the 3Dϕ domain. The iteration sequence is presented in complete detail in Table 3. The previous discussion on the convergence test occurs at step E.2. Note that an additional iterative decision is suggested at step C.3 prior to actual generation of a 3DPNS solution. The sole input parameters are freestream and jet initial velocity, jet diameter, and radius distribution of the jet centerline. All remaining steps require completion of various computational sequences. Therefore, appropriate numerical solution algorithms are required identified.

Finite Element Solution Algorithm

The 3DPNS partial differential equation system, proposed to describe the viscous and turbulent flowfield in the immediate vicinity of a V/STOL jet in crossflow, has been presented. Each member of the equation set (13)-(18) plus (8) and (12) for the complementary and particular pressure fields, belongs to the general class of second-order, non-linear elliptic partial differential equations. Hence, define the generalized dependent variable descriptor $\{q\} \equiv \{\tilde{u}_i, k, \varepsilon, p_C, p_p, \phi\}$, where ϕ is the potential function

describing the exterior three-dimensional potential flow which completes the interaction algorithm. Each governing partial differential equation for $\{q\}$ belongs to the form

$$L(q) = \frac{\partial}{\partial x_\ell}\left[K\frac{\partial q}{\partial x_\ell}\right] + f_1\left(q, \frac{\partial q}{\partial x_\ell}, p, x_i\right) + f_2\left(\bar{u}_1, \frac{\partial q}{\partial x_1}\right) = 0 \qquad (36)$$

In equation (36), the tensor indices range $2 \leq \ell \leq 3$, and $1 \leq i \leq 3$, K is the diffusion coefficient, f_1 is a function of its argument that specifically includes three-dimensional convection, p is any solution parameter including another dependent variable, and f_2 is the initial-value operator if present. The three-dimensional solution of each 3DPNS member of $\{q\}$ is required established on the bounded open domain Ω, formed by the interior to the interaction surface truncated by the injector plate and open at the downstream end.

33

Table 3

ITERATION SEQUENCE FOR V/STOL INTERACTION ALGORITHM

A. SOLUTION PARAMETERS

Input:　　　 U_∞ = freestream velocity

　　　　　　 U_j = initial jet velocity

　　　　　　 d = initial jet diameter

　　　　　　 $\bar{r}(x_i)$ = distribution of jet axis radius

B. GROUND PLANE CONTOUR AND EDGE ENTRAINMENT

Determine:　 S_1 = interaction surface intersection with plate

　　　　　　 $u^\perp$ ≡ entrainment velocity on S_1

　　　　　　 Procedure: a) solve $\nabla^2\phi = 0$ on 2D blockage "airfoil" contours

　　　　　　　　　　　 b) select S_1 with $C_p^b \geq C_p$ everywhere

　　　　　　 Yields:　　 S_1 = initial interface contour

　　　　　　　　　　　 $u^\perp$ = initial contour entrainment velocity

　　　　　　　　　　　 s_j = location of jet inside S_1

C. 3-D POTENTIAL FLOW

1. Determine:　 $S_i(x_1)$ ≡ interaction surface contours at n stations, starting at plate to "sufficienctly" downstream, $1 < i \leq n$.

　　　　　　 Procedure: a) using S_1 and any available data for S_n, interpolate a smooth family of contours.

2. Determine:　 $C_p(S_i)$ ≡ exterior potential flow pressure on $S_i(x_1)$

　　　　　　 Procedure: a) interpolate $u^\perp(x)$ over S_i, $1 < i \leq n$

　　　　　　　　　　　 b) apply as onset velocity boundary conditions

　　　　　　　　　　　 c) estimate u_1 on lid of 3D domain

　　　　　　　　　　　 d) solve $\nabla^2\phi = 0$ on 3D domain

　　　　　　 Yields:　　 $C_p(S_i)$

　　　　　　　　　　　 C_p on injector plate

3. Decision:　　 compare C_p on plate to experimental data(if available)

　　　　　　　　　　　 a) if agreement good, proceed to step D

　　　　　　　　　　　 b) if not, return to C.1, alter S_i and/or $u^\perp$ interpolation

D. 3DPNS SOLUTION INITIATION

1. Determine: $\tilde{u}_i(x_\ell, x_1^o) \equiv$ initial velocity distribution interior to S_1

Procedure: a) $\tilde{u}_1(x_\ell) \equiv \begin{cases} u_j \text{ on } s_j \text{ inside } S_1 \\ \varepsilon > 0 \text{ elsewhere inside } S_1 \end{cases}$

b) solve $\nabla^2 \tilde{u}_\ell = 0$ interior to S_1 boundary conditions provided by resolution of u^b and $u^\perp$ onto $\tilde{u}_\ell(\bar{x}_\ell)$

Yields: $\tilde{u}_i(x_\ell, x_i^o)$

2. Determine: $k, \varepsilon \equiv$ remaining initial-value variable distributions on S_1

Procedure: a) determine $\nabla \tilde{u}_1 \cdot \nabla \tilde{u}_1$ on $S_1(x_\ell)$

b) using MLT concepts, determine ν^e

c) defining length scale, solve for $k(x_\ell)$, $\varepsilon(x_\ell)$

d) set background level of $k > 0$

Yields: $k(x_\ell, x_i^o)$

$\varepsilon(x_\ell, x_i^o)$

$\nu^e(x_\ell, x_i^o)$

3. Determine: $p_c(x_\ell, x_1) \equiv$ complementary pressures on S_i, $1 \leq i \leq n$

Procedure: a) solve $\nabla^2 p_c = 0$ on each S_i

b) store computed pressure distributions

Yields: $p_c(x_\ell, x_1)$

$\nabla p_c(x_\ell, x_1)$

E. 3DPNS JET REGION SOLUTION

1. Determine: 3DPNS solution interior to $S(x_1)$

Procedure: a) integrate 3DPNS equation system on x_1

b) all boundary conditions are known

c) start p_p solution when derivatives available

d) entrainment distributed by continuity

Yields: $\tilde{u}_1, \tilde{u}_\ell, k, \varepsilon, p$ throughout $S(x_1)$ envelope

2. Decision: compatability of 3DPNS and 3Dϕ solutions at S_n

Procedure: a) 3DPNS yields $\tilde{u}_1(\bar{x}_\ell, x_1^n) > 0$ on S_n

b) compare this distribution to potential lid u_1 estimate, C.2.c).

Choice: a) if agreement good, solution is complete

b) if not, return to C.2 for next iteration

35

The three-dimensional potential flow is required determined exterior to the interaction surface and above the injector plate with farfield closure located a sufficiently remote distance. Expressed concisely, the 3DPNS solution domain is

$$\Omega \equiv R^2 x \left[x_0, x \right) \epsilon \; x_\ell \times \left[x_1^o, \; x_1 \right) \tag{37}$$

while the 3Dϕ solution domain is simply $R^3 \epsilon x_i$.

Note in equations (12) and (8), for p_p and p_c, that f_2 vanishes identically and x_1 appears only as a parameter. Independent of this, each 3DPNS equation is an elliptic boundary value description and boundary conditions are required specified on the interface surface at each x_1 station. As a reminder, the closure $\partial\Omega$ of the 3DPNS solution domain Ω is

$$\partial\Omega \equiv \partial R^2 x \left[x_0, \; x \right) \epsilon \; \bar{x}_\ell \times x_1 \tag{38}$$

On $\partial\Omega$, a boundary condition statement that includes all admissible combinations of function and normal derivative constraints is

$$\ell(q) = a_1 \; q + a_2 \; K\frac{\partial q}{\partial x_\ell} \; n_\ell \; + a_3 = 0 \tag{39}$$

where the $a_i(\bar{x}_\ell, x_1)$ are specified. Except for $q = \{p_c, p_p\}$ an initial condition is required at or near the injection surface, i.e. on $R^2 U \partial R^2 \times x_1^o$. The form is

$$q(x_1^o, \; x_2, \; x_3) \equiv q_0(x_2, \; x_3) \tag{40}$$

The finite element numerical solution algorithm for 3DPNS simply assumes all q and p interpolated on the discretization of the solution domain Ω in the form

$$q_e(x_\ell, x) = \{N_k(x_\ell)\}^T \{Q(x)\}_e \tag{41}$$

where the subscript e denotes constrained to the finite element domain $\Omega_e = R_e^2 \times x_1$. Determination of the unknown expansion coefficients $\{q\} \equiv \sum_e \{Q\}_e$, is accomplished using the Method of Weighted Residuals (ref. 20) as

36

$$S_e \left[\int\limits_{R_e^2} \{N(x_\ell)\} \, L(q_e) d\tau - \lambda \int\limits_{R_e^2 \cap \partial R^2} \{N(x_\ell)\} \ell(q_e) d\tau \right] \equiv \{0\} \qquad (42)$$

where S_e is the assembly operator. The assembled finite element algorithm for representative partial differential equation (36), plus boundary condition statement (39) is

$$S_e \left[-\int\limits_{R_e^2} \frac{\partial}{\partial x_\ell} \{N\} \, K \frac{\partial q_e}{\partial x_\ell} d\tau + \int\limits_{R_e^2} \{N\} \, (f_{1e} + f_{2e}) d\tau \right.$$

$$\left. - \int\limits_{\partial R_e^2 \cap \partial R} \{N\} \left[a_1 \, q_e + a_3 \right] d\tau \right] \equiv \{0\} \qquad (43)$$

The subscripts e again denote functions defined on the finite element discretization Ω_e of the global domain Ω.

The rank of equation (43) is identical with the total number of node points on $R^2 U \partial R^2$ at which the dependent variable q requires solution. For f_2 non-vanishing, equation (43) is a system of first-order ordinary differential equations. For f_2 vanishing identically, it is large order algebraic, and the matrix structure is symmetric, sparse and banded. Hence, standard finite element matrix solution methods are applicable for determination of P_c, P_p, and ϕ.

An implicit numerical integration is employed to solve equation (43) for all initial-value problem descriptions in 3DPNS. The explicit form of equation (43) is, in this instance,

$$S_e \left[[C]_e \{q\}'_e + ([U]_e + [K]_e) \{Q\}_e + \{f\}_e \right] \equiv \{0\} \qquad (44)$$

The superscript prime denotes the ordinary derivative with respect to the x_1 (η_1) coordinate. The matrix expressions for the first three terms, which account for axial convection, and transverse plane convection and diffusion respectively, are

37

$$[C]_e \equiv \{\bar{\rho}\ddot{u}_1\}_e^T \int\limits_{R_e^2} \{N\}\,\{N\}\,\{N\}^T d\tau$$

$$[U]_e \equiv \{\bar{\rho}\tilde{u}_\ell\}_e^T \int\limits_{R_e^2} \{N\}\,\{N\}\,\frac{\partial\{N\}}{\partial x_\ell}\,d\tau \tag{45}$$

$$[K]_e \equiv \{\bar{\varepsilon}\nu^e\}_e^T \int\limits_{R_e^2} \{N\}\,\frac{\partial\{N\}}{\partial x_\ell}\,\frac{\partial\{N\}}{\partial x_\ell}\,d\tau$$

Summation on $2 \leq \ell \leq 3$ is implied, and derivatives on x_j are replaced by equations (26) in the sequel. All terms not explicitly involving q, i.e. $\{Q\}$, are contained in $\{f\}_e$.

A single-step, implicit numerical integration algorithm is employed.

$$\{Q\}_{j+1} = \{Q\}_j + h\left[\theta\{Q\}'_{j+1} + (1-\theta)\{Q\}'_j\right] \tag{46}$$

In equation (46), j is the jet axis station index, h is integration step-size Δx_1, and θ equals one-half yields the trapezoidal rule. Following the usual matrix manipulations, insertion of equation (44) into (46) yields a large order, non-linear algebraic equation system. The Newton matrix iterative algorithm for solution of this system is employed as

$$\left[J\left(\{Q\}_{j-\ell}\right)\right]\{\delta Q\}_{j+1}^{p+1} = -\left\{F\left(\{Q\}_{j+1}^p\right)\right\} \tag{47}$$

The dependent variable in equation (47) is the iteration vector, and

$$\{Q\}_{j+1}^{p+1} \equiv \{Q\}_{j+1}^p + \{\delta Q\}_{j+1}^{p+1} \tag{48}$$

where p is the iteration index, and $\ell < 0$ is an integer that can retard evaluation of the Jacobian as an economy measure. The right side of equation (47) is the homogeneous form of equation (46) evaluated with the p<u>th</u> iterate, i.e.

38

$$\{F\}^p_{j+1} = S_e \left[[C]_e \left(\{Q\}^p_{j+1} - \{Q\}_j \right) + h \left(\theta\{g_e\}^p_{j+1} + (1 - \theta)\{g_e\}_j \right) \right] \qquad (49)$$

where

$$\{g_e\}^p_\ell \equiv ([U]_e + [K]_e) \{Q\}^p_\ell + \{f\}_e \qquad (50)$$

Equations (49)-(50) are defined only in terms of inner products on elements, with the assembly operator yielding the equivalent global expression. The vanishing of {F}, to within definition of a computed zero, yields equation (47) homogeneous, hence convergence of the iteration for any evaluation of the Jacobian. The initial estimate $\{Q\}^1_{j+1}$ for any iteration can be determined using $\theta = 0$.

By definition, the Jacobian is the derivative of equation (49) with respect to $\{Q\}^p$. It is computationally evaluated as

$$[J] = S_e \left[[C]_e + h\theta([K]_e + [U]_e) \right] \qquad (51)$$

All operations are again limited to matrix inner products on an elemental basis. The rank of $[J]$ equals the order of $\{\delta Q\}$; specific (Dirichlet) boundary constraints are applied within the evaluation of {F}.

39

Test Case

As apparent from Table 3, the developed viscous-inviscid three-dimensional interaction algorithm for V/STOL jet flowfield prediction requires substantial computational capabilities. The immediate requirement is to assess the pivotal elements of the algorithm to evaluate its intrinsic viability and usefulness. The circular jet, injected perpendicular to the plate and to the crossflow represents the basic geometry and a substantial experimental data base exists. Therefore, computational tests were conducted for a normal circular jet at $\lambda = 8$ and $d_j = 0.05$ m (2 in.). The data of Mosher (ref. 10), also Fearn and Weston (ref. 13), provide plate C_p distributions for Step B comparisons, and the downstream interface shape for Step C can be estimated from ref. 12, for the case of $U_\infty = 15$ m/s (50 f/s). Equation (30) provides the remaining Step A input requirement $\bar{r}(x_1)$.

Ground Plane Interface Contour

The first requirement of the algoritm is determination of a geometry for the intersection of the viscous-inviscid interaction surface with the injector plate, Step B of Table 3. The contour determined may not be unique, but the existence of at least one contour is mandatory. Viewing Figure 3, the assumption is that the blockage-only contour is an elementary airfoil belonging to the Karman-Trefftz family. The adjustment parameters are thickness ratio and trailing edge included angle, and the airfoil may not close at the trailing edge. The comparison plate pressure distributions are shown in Figure 13. The position of the jet within the contour is also an unknown to be determined.

The computational capability to conduct the two-dimensional solutions exists in the COMOC computer program (ref. 22). Figure 14 illustrates a representative macro-element discretization, with boundary condition specifications noted thereon, and the resultant finite element computational grid generated by the program. From Figure 14, a large thickness ratio appears required for the contour, yet pressure recovery in the trailing edge region must be modest. Figure 15 summarizes the results of tests, conducted with large thickness ratios and large closed trailing edge angle, to serve as a comparison basis. A large negative pressure region is induced, but trailing edge recovery is much too large. The next step assessed recovery modification by opening the trailing edge to simulate the anticipated blunt base requirement. Figure 16 summarizes the results, which indicate smaller trailing edge recoveries can be acheived but remain unacceptably high.

Reviewing these data indicates that a segment of the assumed airfoil contour, from the trailing edge forward to some x/C, must lie beyond the interaction contour footprint on the plate. To ascertain this, the experimental
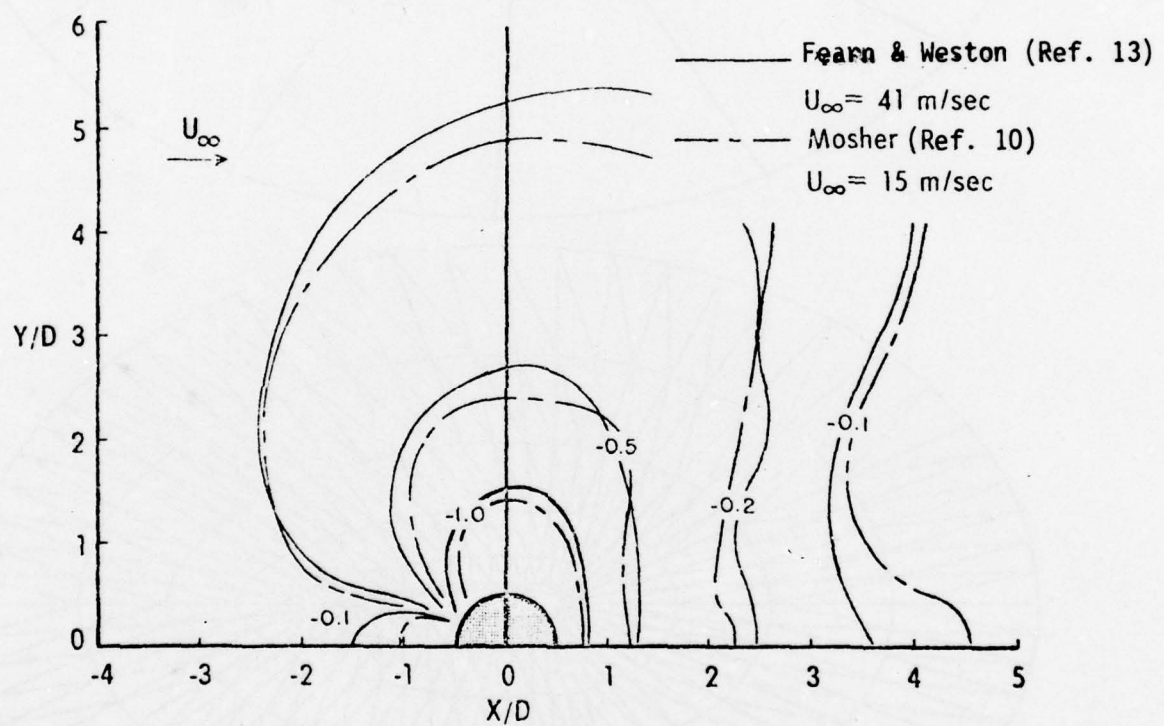
Figure 13.   Experimental Contours Of Constant Surface Pressure
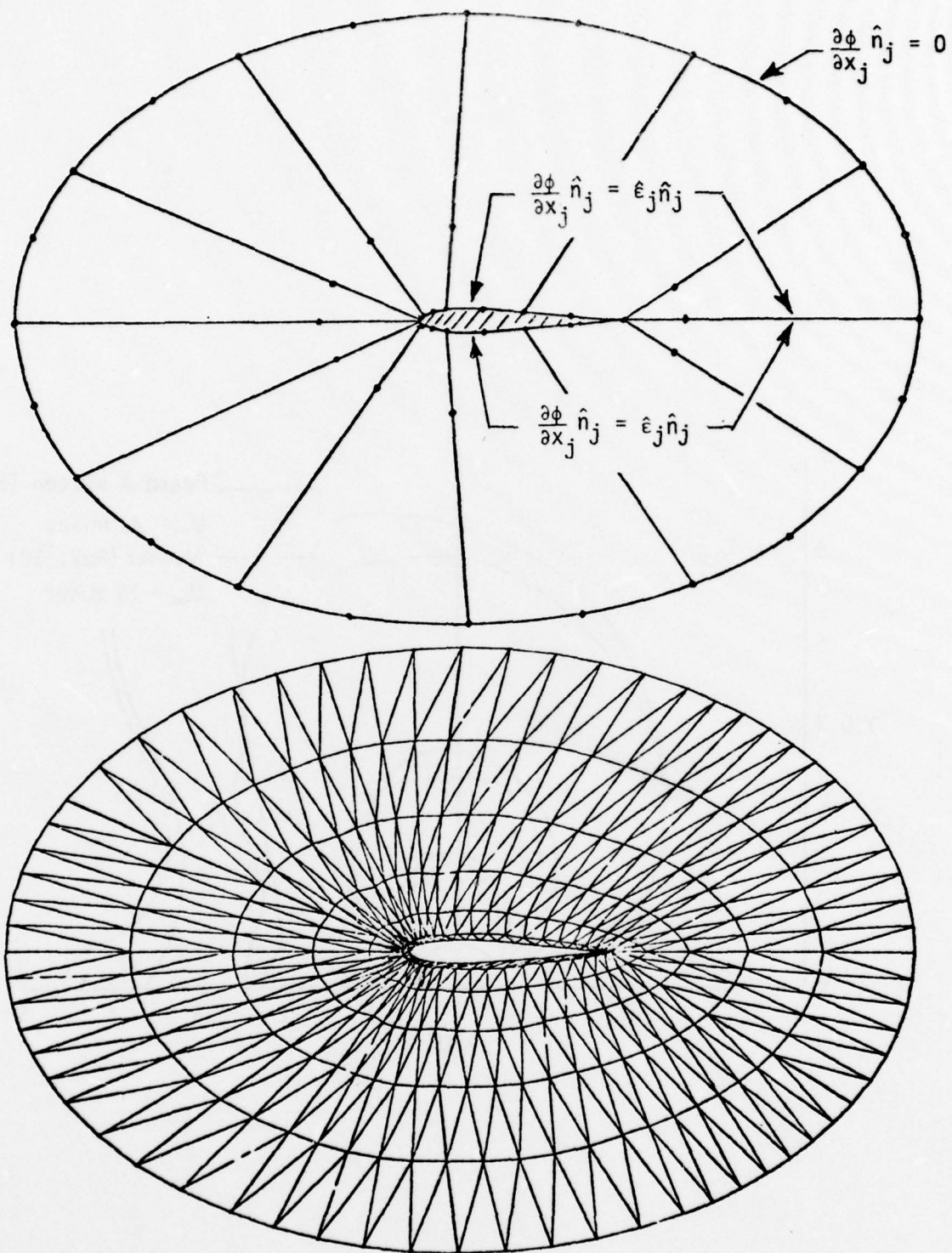Distributions For Circular Jet, $\lambda = 8$.

41

Figure 14. Macro Element And Finite Element Discretizations For
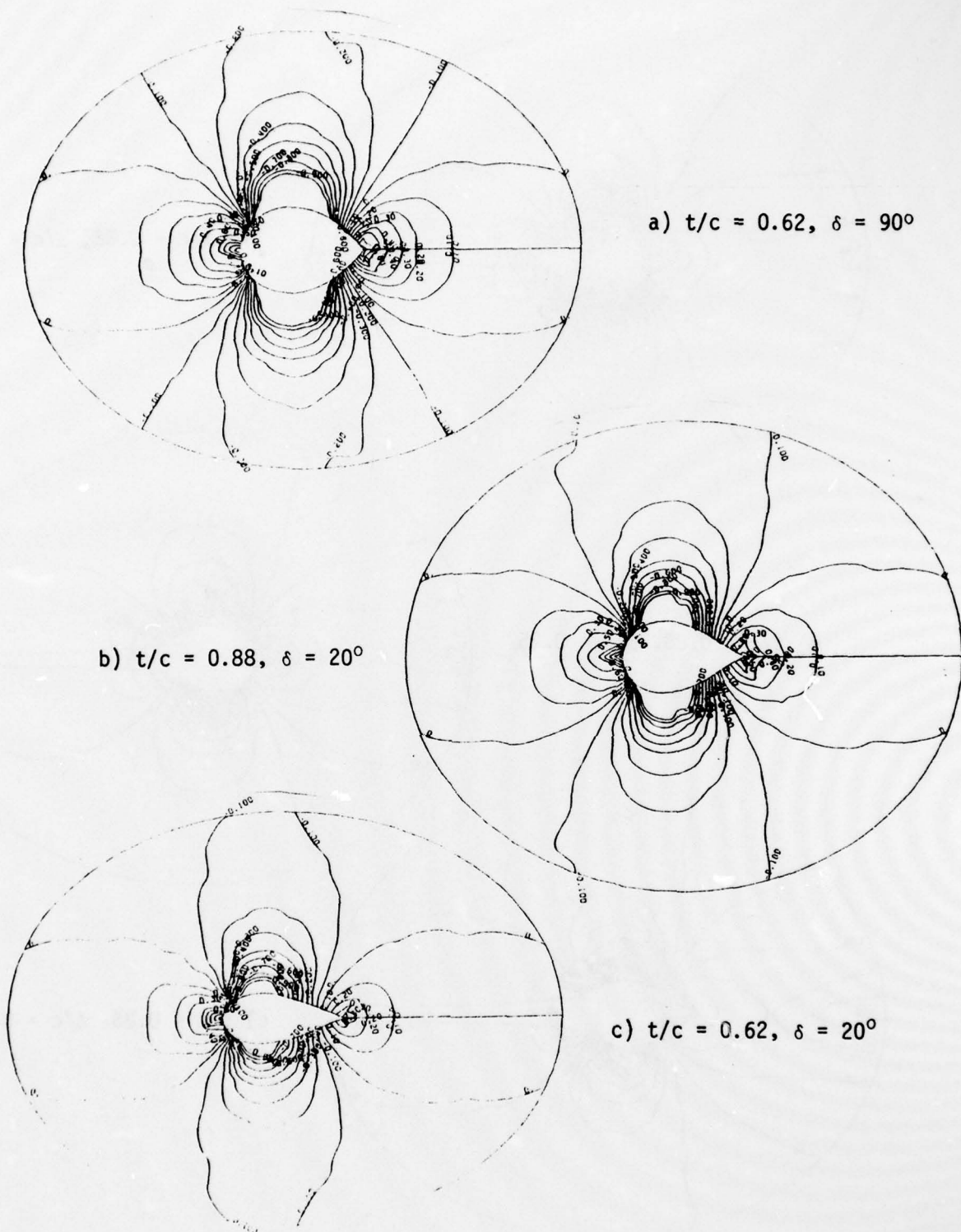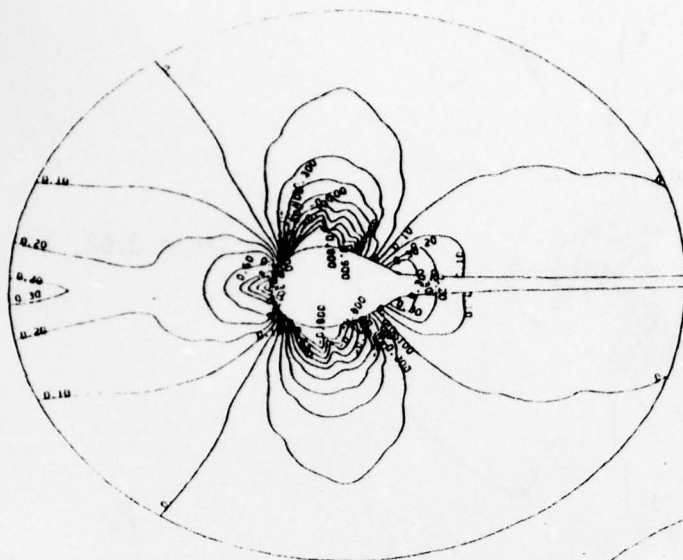Karman-Trefftz Potential Solutions

a) t/c = 0.62, δ = 90°

b) t/c = 0.88, δ = 20°

c) t/c = 0.62, δ = 20°

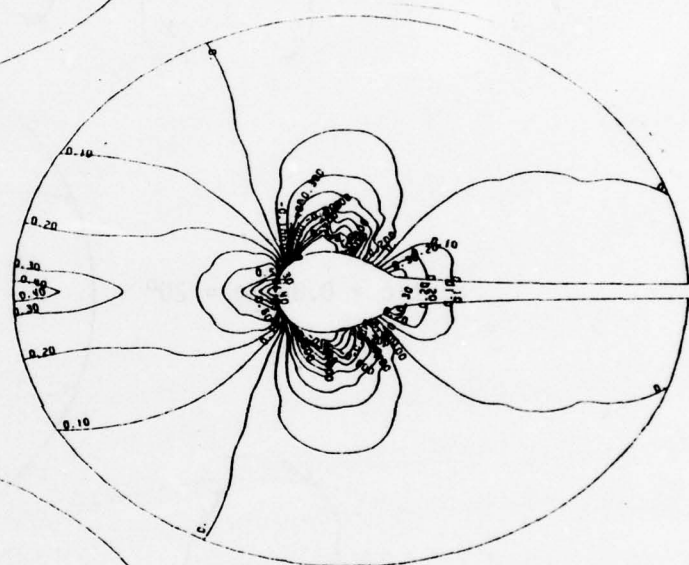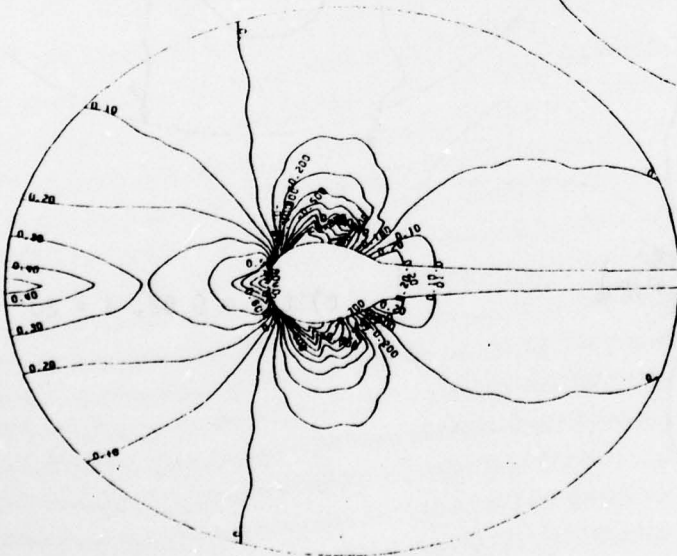Figure 15.   Computed Inviscid Pressure Distributions For Various Closed
Trailing Edge Angles

43

a) t/c = 0.88, Δ/c = 0.10

b) t/c = 0.88, Δ/c = 0.25

c) t/c = 0.88, Δ/c = 0.40

Figure 16.   Computed Inviscid Pressure Distributions For Various
Open Trailing Edge Airfoils

44

pressures were interpolated to determine C_p vs. x/C on various thickness ratio airfoil contours, as illustrated in Figure 13, assuming a larger than required chord. The blockage-only pressure distribution C_p^b on each contour was then computed for various thickness ratios and trailing edge included angle and gap. A summary of results is shown in Figure 17. The 35% thick airfoil, with vanishing trailing edge angle and gap, and with the last 35% of chord discarded met the requirements of Step B. By moving the center of the jet just downstream of its assumed initial coordinate, Figure 17e, it became possible to completely envelope the computed C_p^b with the experimental C_p. The downstream intersection of these two curves determined the truncation point of the airfoil.

Therefore, for this jet test case at least, it is possible to determine an aerodynamic blockage-only contour that meets the requirement of the interaction algorithm. The truncated airfoil contour is completed by dropping a perpendicular segment to the center line axis. The local differences between C_p^b and C_p yield the corresponding entrainment velocity distribution $u^\perp$ using equation (4). Furthermore, the jet has become located within the domain. Hence, all requirements of Step B., Table 3 have been met.

Blockage Plus Entrainment Potential Solution

Step C, the next computational sequence in the algorithm, has as its primary requirement the determination of the inviscid pressure distribution on the entire interaction surface. Recalling equations (7)-(10), the 3DPNS solution is coupled to the $3D\phi$ solution via the complementary pressure distribution, the boundary condition for which is the inviscid pressure. For the test case, the interaction surface contour at $x_1/d = 0$, after truncation, is equal to 3.2d and the thickness equals 0.7d.

The interface surface is interpolated with the assistance of any available data. Figure 18 illustrates a three-dimensional finite element discretization of the $3D\phi$ solution domain, where the interface surface $S_1(x_1)$ has been smoothly interpolated over $0 < x_1/d < 5.2$. The second requirement for the $3D\phi$ solution is distribution of the entrainment velocity onto $S(x_1)$. Experiment indicates it vanishes by $x_1/d = 5.2$, and in the absence of other data, a linear distribution was assumed.

The computational requirement for Step C is solution of the three-dimensional potential flow equation on the domain shown in Figure 18, subject to the entrainment boundary conditions. The basic capability to solve this system is resident within finite element structural analysis codes, and the SAP program was utilized (ref. 23). Only indicative results are obtainable, however, since the (displacement) vector dependent variable character of elasticity requires "interpretation" to run the scalar variable ϕ. This was accomplished by equating ϕ to the z-component of displacement and specifying the (x, y) plane entrainment. The non-zero z entrainment component, required for Step E.2 could not be specified.

45

a) t/C = 0.38, δ = 20°, Δ/C = 0.16

b) t/C = 0.38, δ = 20°, Δ/C = 0

c) t/C = 0.25, δ = 20°, Δ/C = 0

d) t/C = 0.25, δ = 40°, Δ/C = 0

e) t/C = 0.35, δ = 0°, Δ/C = 0

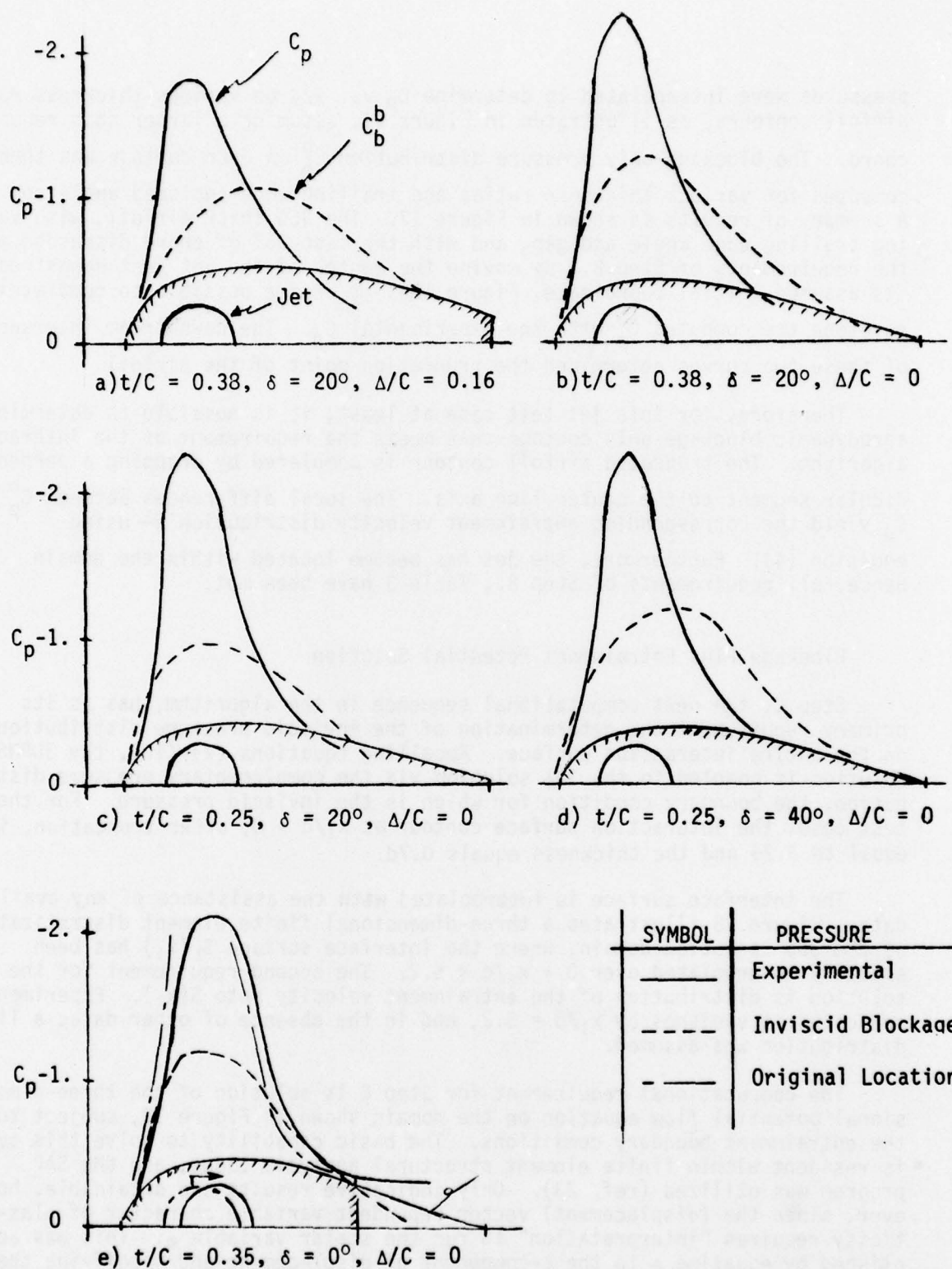| SYMBOL	PRESSURE
	Experimental
	Inviscid Blockage
	Original Location

Figure 17.   Computed Pressure Coefficient Distributions On Various
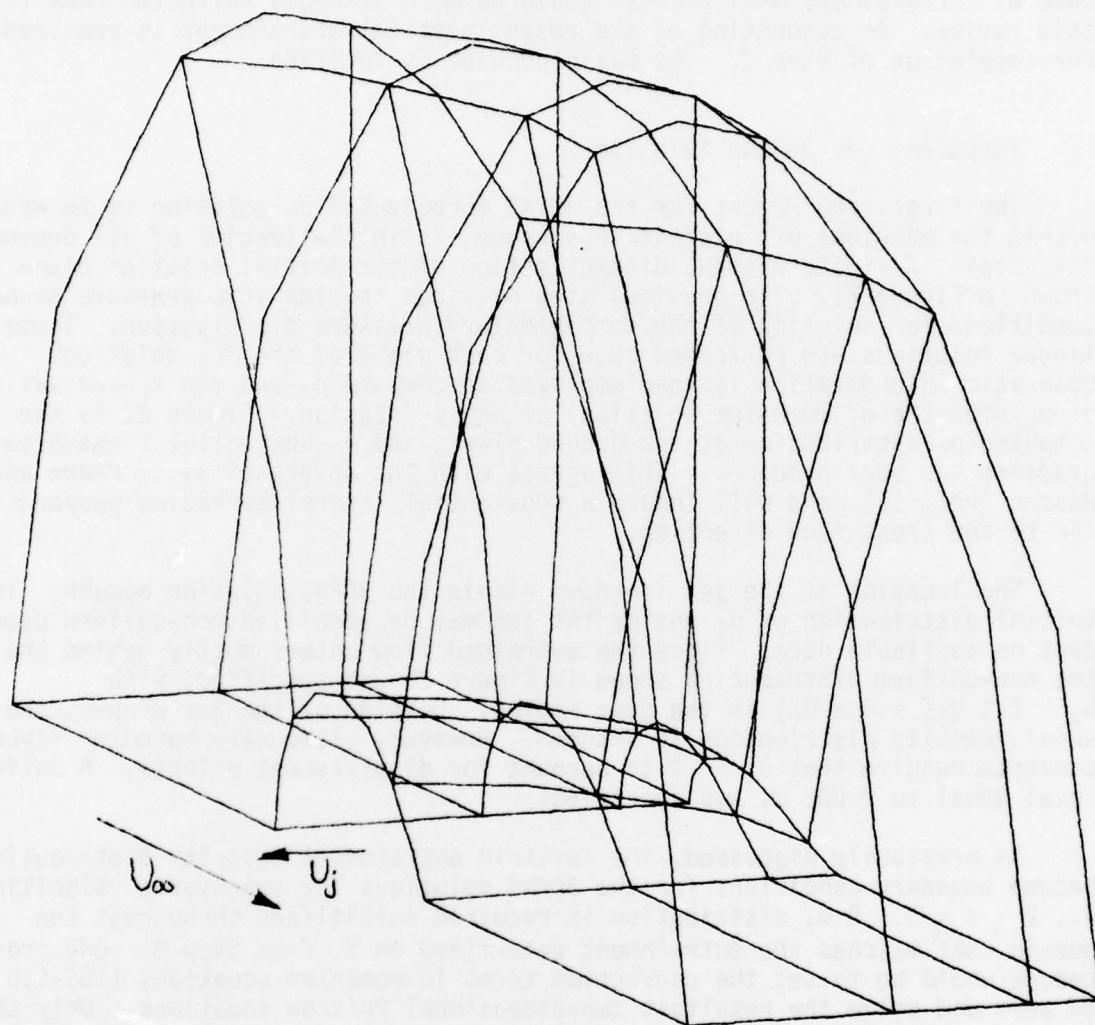Interface Geometries, Circular Jet, λ = 8

Figure 18. Three-Dimensional Potential Flow Solution Domain For

Circular Jet, $\lambda = 8$, $U_\infty = 15$m/s

Within these constraints, a 3Dϕ solution was obtained using SAP for the specified interface contour and entrainment distributions. Figure 19 illustrates this solution with ϕ plotted as z-displacements superimposed on computational grid planes. The computed pressure distribution on the injector plane is shown in Figure 20. Agreement with the experimental data is quite good in the near vicinity of the interface contour, see Figure 13. The influence of three-dimensional effects would be more strongly reflected away from this region. An accounting of the absent vertical entrainment is required for completion of Step C. The basic concept is verified.

Turbulent Jet Region Solution

The first requirement for the 3DPNS turbulent flow solution to be obtained within the envelope of interaction surface, is initialization of all dependent variables. A finite element discretization of the initial solution plane is shown in Figure 21. The previous step provides the inviscid pressure boundary conditions for solution of the complementary pressure distribution. These linear solutions are performed once for each plane of the 3Dϕ solution. Quadratic interpolation is then employed to compute p_c and the x_1-derivative of p_c (for the $\tilde{u}_1$ momentum equation) at any x_1 station. Figure 22 is the computed p_c distribution at the ground plane, and a substantial transverse gradient has been produced. This agrees with the observations of Fearn and Weston (ref. 13), and will induce a substantial lateral spreading perpendicular to the cross-flow direction.

The location of the jet is known within the 3DPNS solution domain. The initial distribution of $\tilde{u}_1$ inside the jet may be specified non-uniform dependent on available data. Since the entrained flow enters mostly behind the jet, the non-uniform distribution shown in Figure 23 was specified, with $\tilde{u}_1 \approx 1.1\ U_j(\ = 8.8\ U_\infty)$ in the near region. Outside of the jet proper, the axial velocity distribution is unknown. However, elementary boundary layer concepts require that $\tilde{u}_1 > 0$ to account for displacement effects. A uniform level equal to 0.001 U_∞ was specified.

As previously discussed, the inviscid entrainment velocity distributions become boundary conditions for the 3DPNS solutions for transverse velocities $\tilde{u}_\ell$, $2 \leq \ell \leq 3$. A $\tilde{u}_\ell$ distribution is required initialized throughout the domain that matches the entrainment determined on S_1 from Step B. One procedure would be to set the convection terms in momentum equations (15)-(16) to zero and solve the resultant two-dimensional Poisson equations. Only the transverse complementary pressure gradients $\partial p_c / \partial x_\ell$ are known, however, since the Reynolds stresses involve the unknown turbulence kinetic energy and dissipation distributions, k and ε see equations (21). The level of k is probably small everywhere in comparison to that on the periphery of the jet, however, so a first order approximation is to solve the Laplacian for each $\tilde{u}_\ell$ subject to the entrainment boundary conditions. Figure 24a shows the resultant distribution of $\tilde{u}_\ell$ on S_1 in the form of a vector plot. The action of entrainment is quite noticeable. For comparison, Figure 24b is the same solution with $u^\perp \equiv 0$ on S_1.
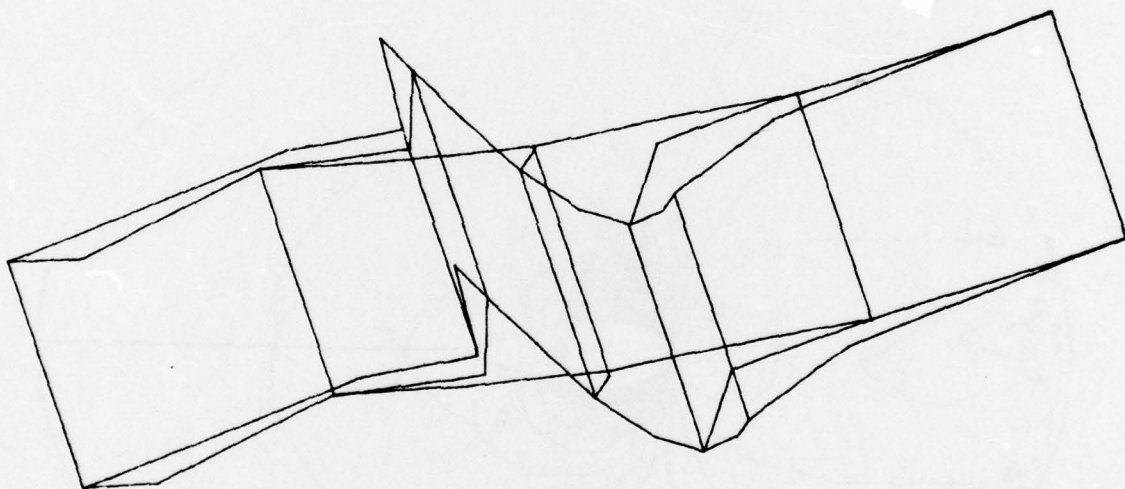
Figure 19. Three-Dimensional Potential Solution
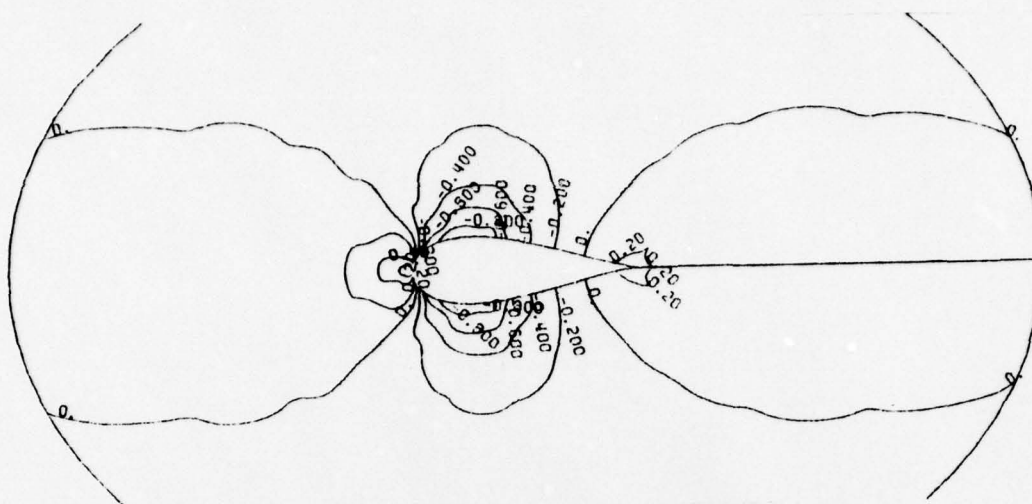
a.) Blockage flow, (no entrainment)
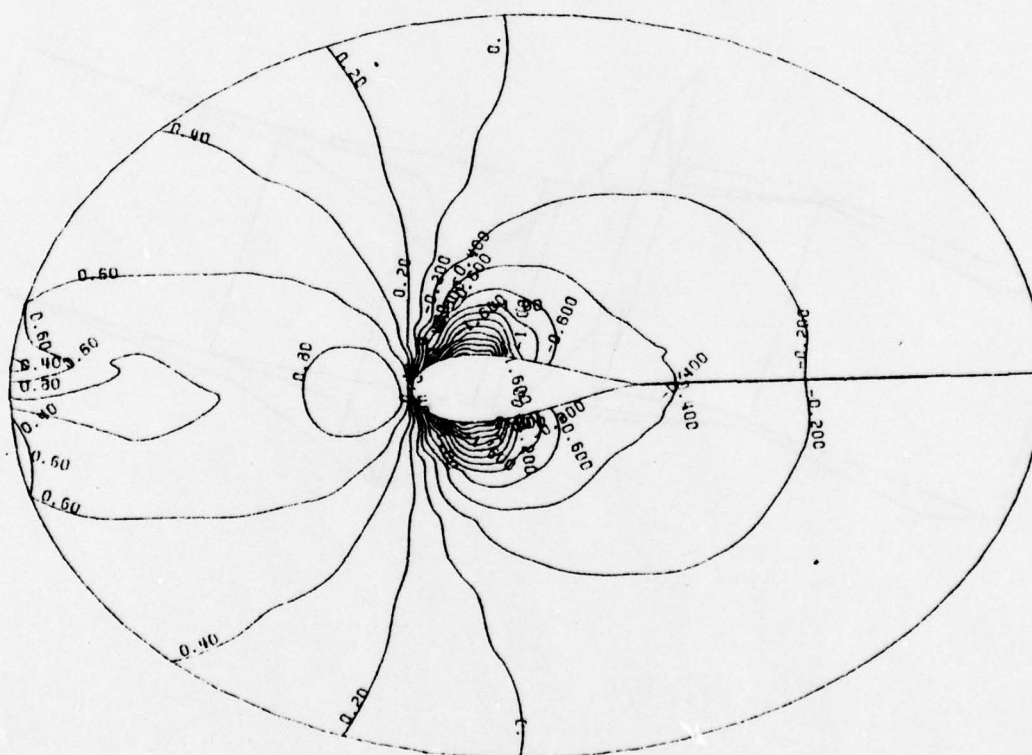
b.) Circular Jet with Entrainment, $\lambda = 8$

Figure 20.   Computed Pressure Distribution On Injection Plane

Figure 21   Generated Finite Element Discretization Of 3DPNS Solution Domain

51

Figure 22. Computed Complementary Pressure Distribution On 3DPNS

Domain at S_1

Figure 23. Initialized Distribution of 3DPNS Axial Velocity $\tilde{u}_1$ on S_1

53

a) With Entrainment from Step B

b) Without Entrainment

Figure 24   Computed Transverse Plane Velocity $\tilde{u}_\ell$ Vector Distributions on S_1

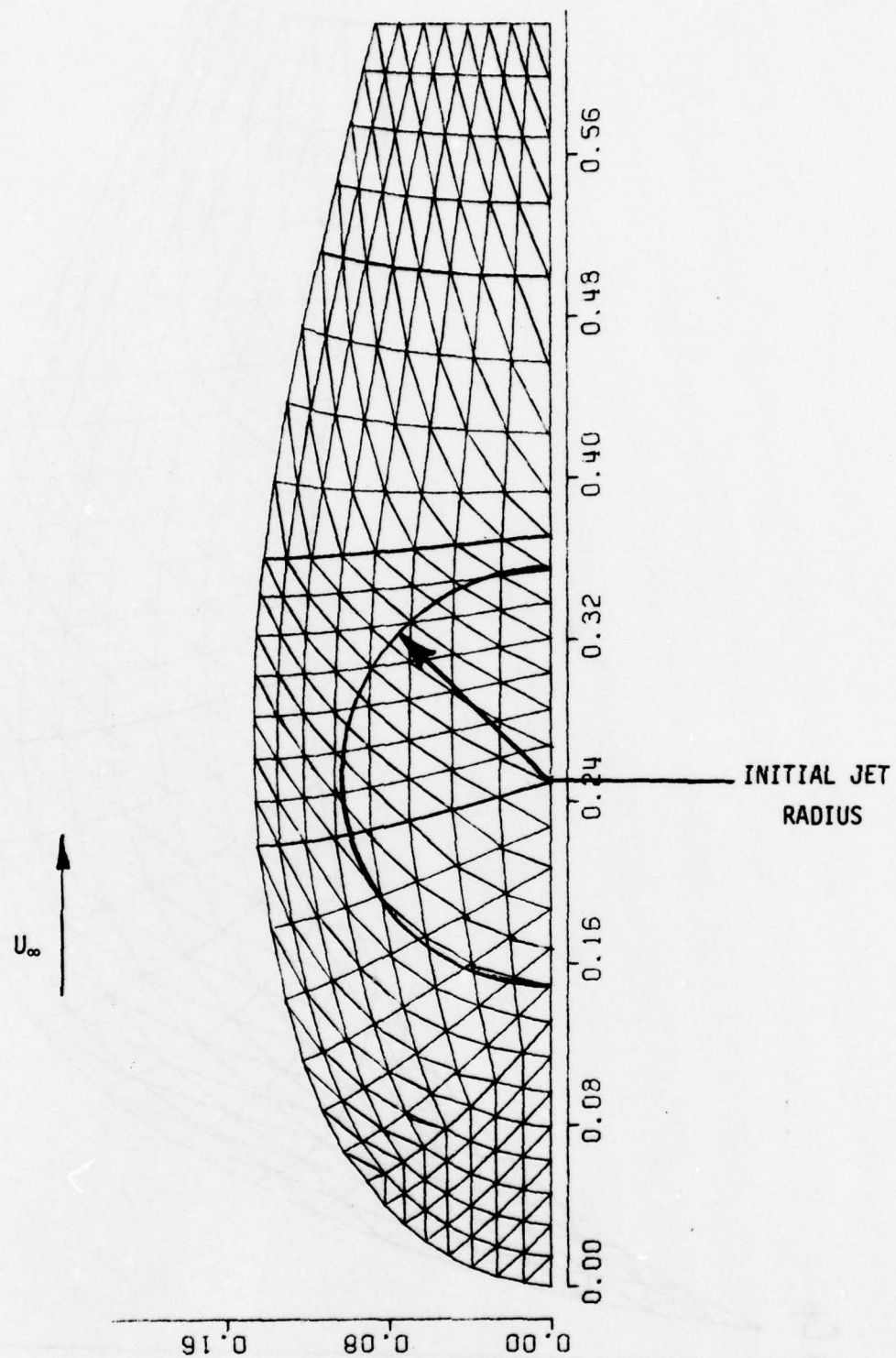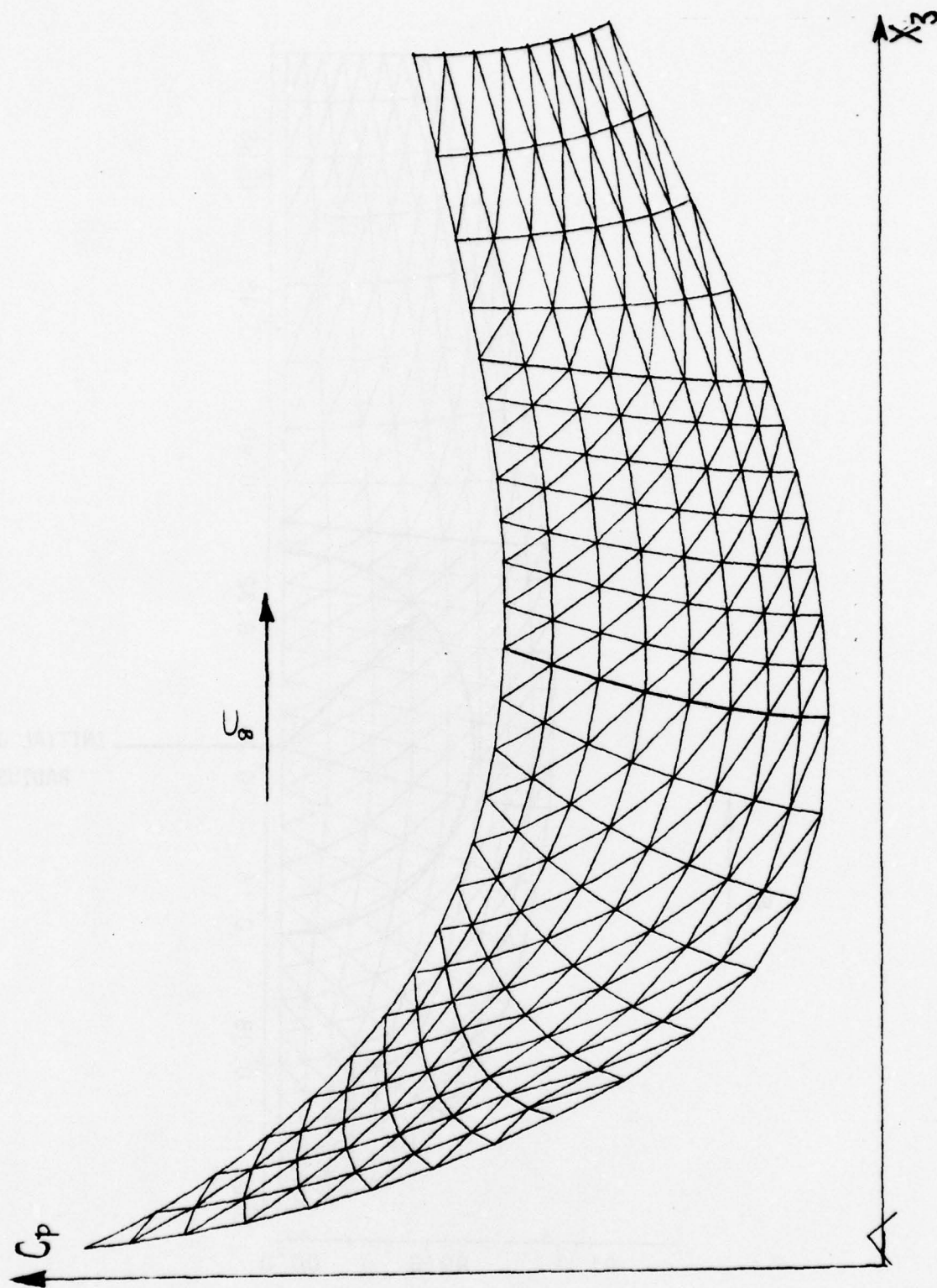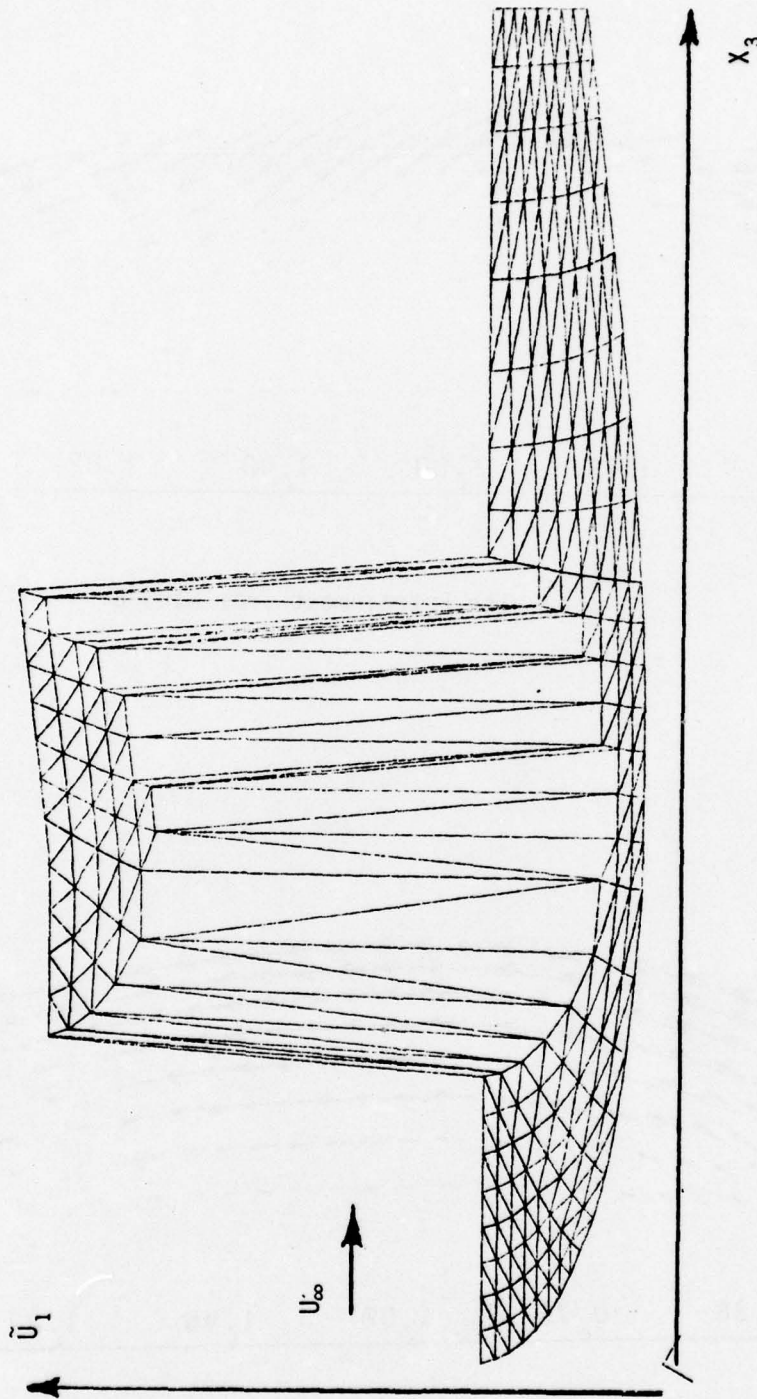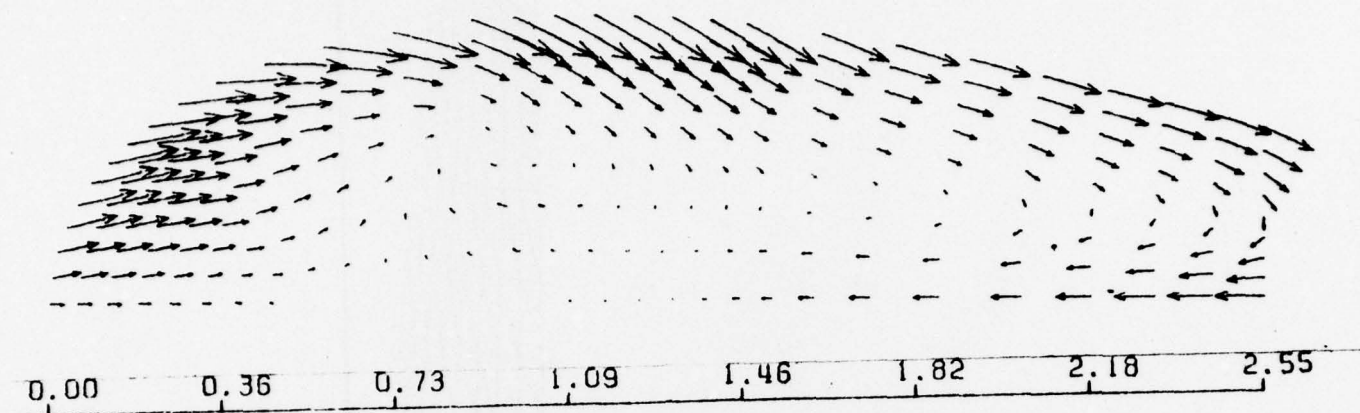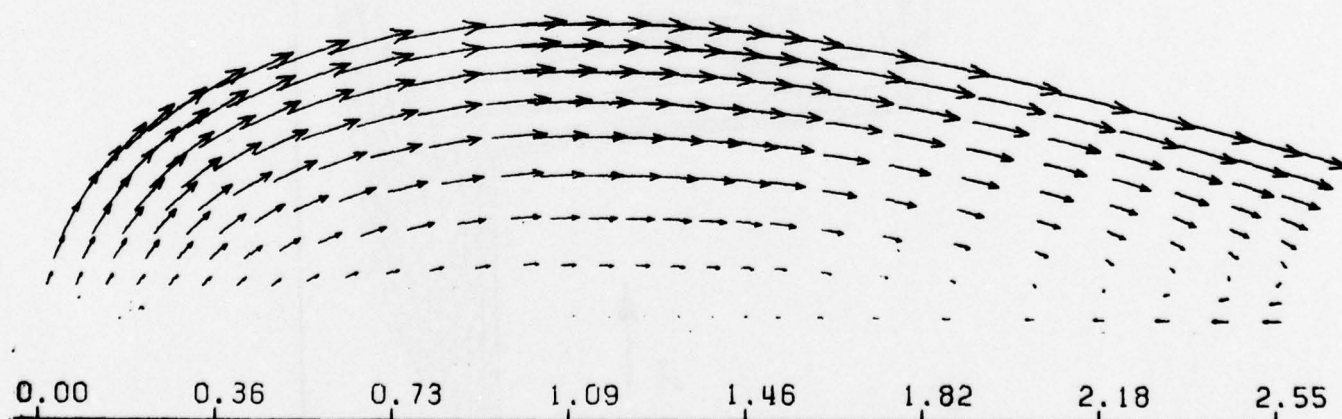Once the mean flow velocity distributions are established, the initial distributions of k and ε can be determined using an adaptation of mixing length theory to estimate local shear stress plus definition of a dissipation length scale. Recall that for an elementary two-dimensional boundary layer flow the dominant Reynolds stress is evaluated as

$$-\overline{u_1' u_2'} \equiv \omega^2 \ell^2 \left[\frac{\partial u_1}{\partial x_2} \right] \tag{52}$$

where ω is Van Driest wall damping and ℓ is the mixing length (cf., ref. 20). Comparing equations (21) and (52), and generalizing the mean shear evaluation, yields

$$C_4 \frac{k^2}{\varepsilon} \approx \omega^2 \ell^2 \left[\frac{\partial \tilde{u}_1}{\partial x_\ell} \frac{\partial \tilde{u}_1}{\partial x_\ell} \right]^{\frac{1}{2}} \tag{53}$$

The additional required relation to solve for a unique k and ε is the dissipation length scale ℓ_d,

$$\ell_d \equiv C_\nu \frac{k^{3/2}}{\varepsilon} \tag{54}$$

where C_ν is a correlation coefficient. Using the bi-derivative evaluation option in COMOC III, assuming a constant ℓ_d that scales the non-dimensional computed $k \leq 1\%$, and assuming a uniform background level of $\sim .01\%$ yields the initial distribution of turbulence kinetic energy shown in Figure 25. Notice the non-negligible levels essentially coincide with the jet periphery.

This computational operation completes the 3DPNS solution initiation sequence specified in Step D, Figure 3. All required information and data are now on hand for execution of the 3DPNS solution, Step E. The entrainment aspects of the interaction algorithm require a restatement of the finite element numerical solution algorithm to account directly for the continuity equation (13) in the solution of equation (14) for $\tilde{u}_1$. Equation (31) is the expansion of the latter in the cylindrical coordinate system. For constant density, the similar expansion for equation (13) is

$$L(\bar{\rho}) = \frac{1}{r} \frac{\partial \tilde{u}_\theta}{\partial \theta} + \frac{1}{r} \frac{\partial (r \tilde{u}_r)}{\partial r} + \frac{\partial \tilde{u}_z}{\partial z} = 0 \tag{55}$$

Both equations (31) and (55) contain the axial derivative of the predominant velocity $\tilde{u}_\theta$ as an unknown. The transverse plane velocity distributions $\tilde{u}_\ell$ have been initialized by the combined action of blockage and entrainment with the latter the mechanism for mass influx into the 3DPNS domain. The associated added mass flux must exit the 3DPNS domain only in the direction parallel to $\tilde{u}_\theta$; hence, equation (55) represents a source for $\tilde{u}_\theta$ and a
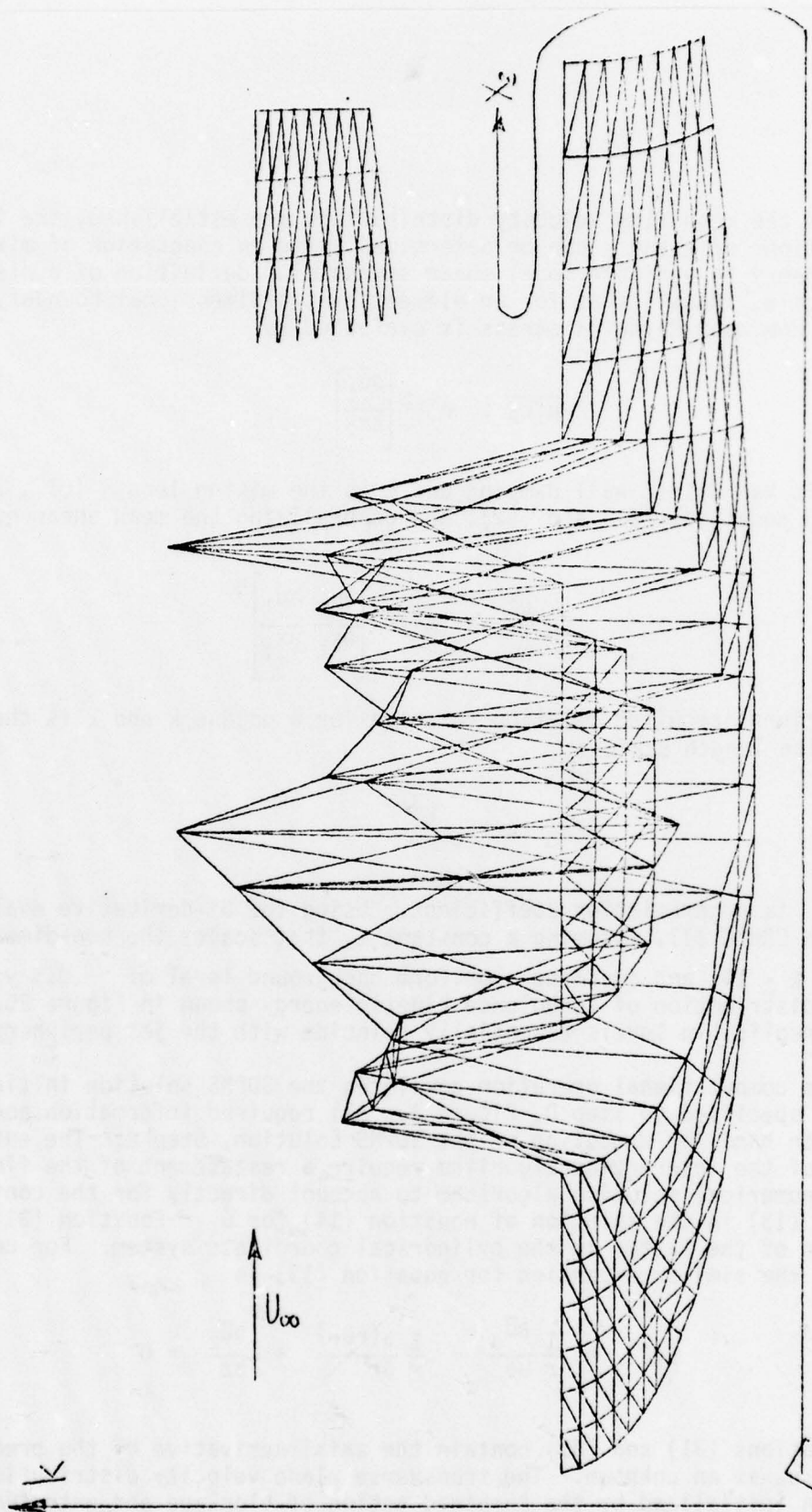
Figure 25. Computed Initial Distribution Of Turbulence Kinetic Energy On 3DPNS Domain

differential constraint on the solution of equation (31). This is accounted for within the finite element solution algorithm in the manner equivalent to use of Lagrange multiplier α. Hence, the algorithm statement of equation (42) for $\tilde{u}_\theta$ becomes

$$
S_e \left[\int_{R_e^2} \{N(x_\ell)\} \; L \; (\tilde{u}_\theta) d\tau - \alpha \int_{R_e^2} \{N(x_\ell)\} \; L(\bar{p}) d\tau \right.
$$

$$
\left. - \lambda \int_{\partial R_e^2 \cap \partial R^2} \{N(x_\ell)\} \; \ell \; (\tilde{u}_\theta) \; d\tau \right] \equiv \{0\} \tag{56}
$$

The first step in the 3DPNS solution is evaluation of the x_1 derivatives of the dependent variable vector $\{q\}$. The $\tilde{u}_1$ velocity field is of greatest interest, and Figures 26-27 are plots of the derivatives computed by equation (56), for $\alpha = 1$ and $\alpha = 0$ (no entrainment). The sole action in the $\alpha = 0$ case is to retard the jet core and accelerate the periphery. However, for $\alpha \neq 0$, an acceleration is induced everywhere by the action of continuity in equation (56). Figure 28 shows the $\tilde{u}_1$ distribution computed within the jet region after proceeding one-half diameter downstream, i.e. parallel to the x_1 axis. The entrainment and complementary pressure boundary conditions previously established in Steps B and C were employed. This action has accelerated the $\tilde{u}_1$ velocities lying on the interfacial surface by ~ 10% U_∞. The required step at this station would be comparison to the entrained 3Dϕ solution. If agreement was satisfactory the 3DPNS solution is continued. If not, the algorithm would be cycled to Step C and the 3Dϕ solution recalculated with an adjusted exit velocity parallel to x_1. This requires formal establishment of the specific 3Dϕ solution capability. For the $\tilde{u}_1$ velocity distribution in Figure 28, the increase in mass flux over that at the initial solution plane is 11%, as determined by integration of the computed $\tilde{u}_1$ distributions over the transverse plane.
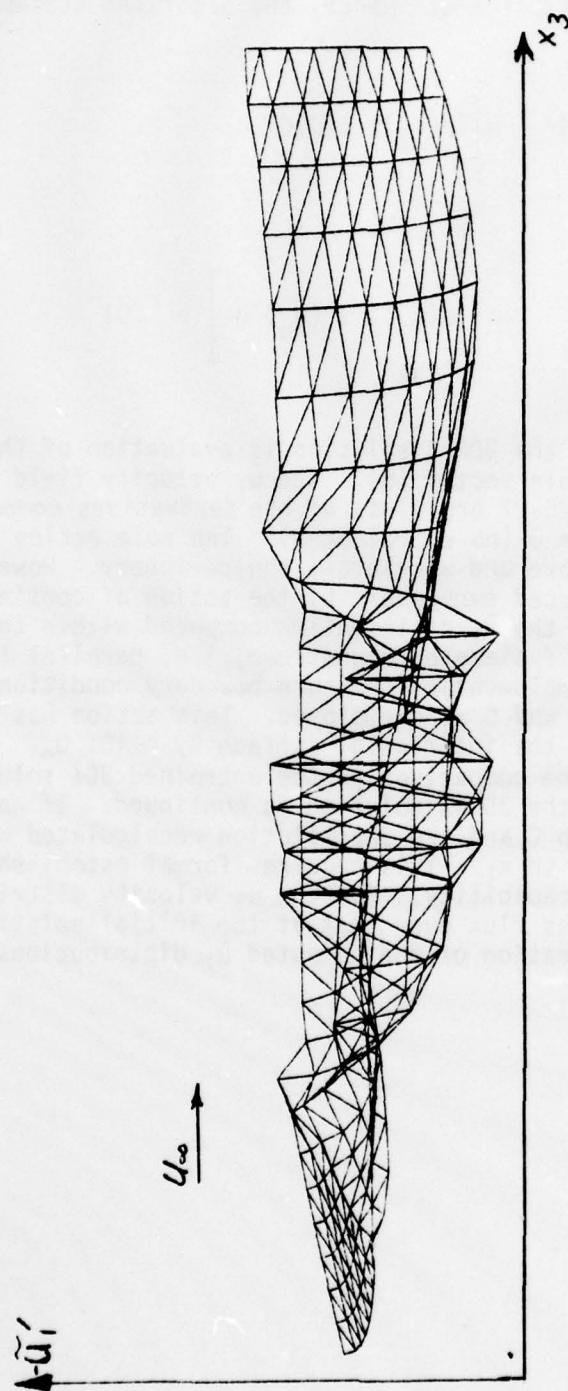
Figure 26. Computed Axial x_1 Derivative Distribution Of Jet Region Velocity

$\tilde{u}_\theta$ On S_1 With Entrainment
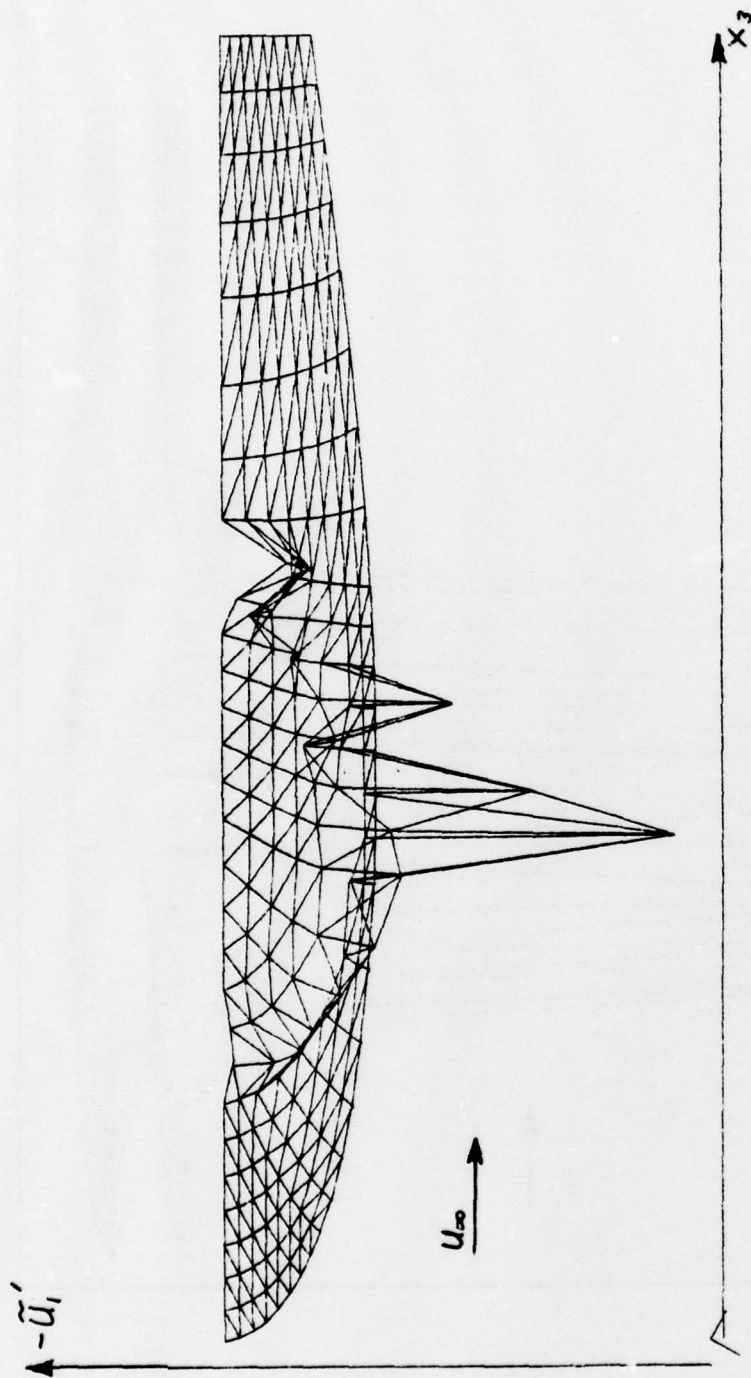
Figure 27. Computed Axial x_1 Derivative Distribution Of Jet Region.Velocity $\tilde{u}_\theta$ On S_1 Without Entrainment
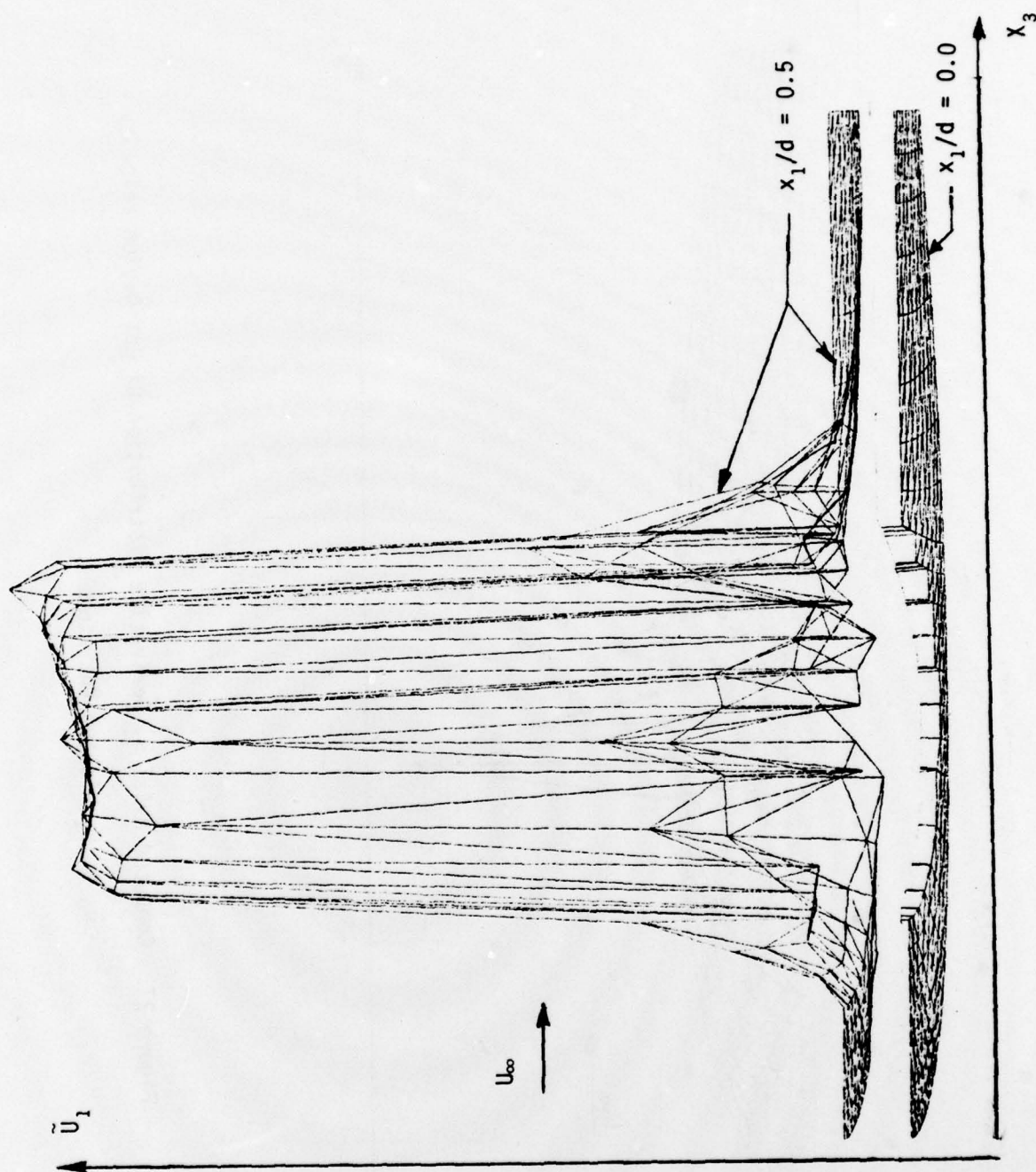
59

Figure 28.   Computed Distribution Of Jet Region Velocity $\tilde{u}_\theta$ On S_2, $x_1/d = 0.5$

SUMMARY & CONCLUSIONS

A viscous-inviscid interaction algorithm has been derived for numerical determination of the detailed three-dimensional flowfield surrounding and entrained into the wake of a V/STOL jet issued orthogonally into a subsonic crossflow bounded on one plane by an aerodynamic surface. The dominant influence parameter coupling the three-dimensional external potential flow analysis, and the imbedded three-dimensional viscous and turbulent analysis of the jet and nearfield wake, is the entrainment flow induced into the jet region and its influence on the potential flow. The two distinct solution domains are pressure coupled and the entrainment-induced mass flux addition to the wake is the primary iteration variable of the global algorithm.

A key element of the algorithm is definition of a surface defining the coincident boundary of the dual analyses. Numerical studies have confirmed existence of the interface surface for the test case of a circular jet issued into a crossflow with velocity ratio equal to eight. This determination yields definition of the specific geometry of the interface intersection with the injection plane and the entrainment velocity distribution thereon. Any experimental surface pressure data may be specifically employed in this analysis phase, and may in addition be used to complete definition of the interface surface evolution. The summary three-dimensional jet region computations yield determination of the detailed evolution of the turbulent flow and employ a turbulence closure model involving all six components of the Reynolds stress tensor. Finite element numerics have been employed to computationally evaluate the five distinct computational phases of the algorithm.

Several additional numerical developments are required completed to fully assess the generality of the developed interaction algorithm. Specifically:

1. A three-dimensional potential flow analysis with entrainment is required established to complete assessment of convergence of the dual analyses to a unique velocity field. The specific requirement is to be able to specify onset velocity distributions on all surfaces of the domain boundary and to generate the resultant three-dimensional potential flow distribution.

2. Having acheived completion of the development specified in 1. above, additional numerical solutions for the perpendicular circular jet are required to assess factors related to convergence.

3. The versatility of the interaction algorithm is required assessed by application to non-perpendicular injected circular jets and to rectangular jets of practical aspect ratio. The required experimental data on (primarily) surface pressure distributions are available.

4. The compromising influence induced into the three-dimensional turbulent jet region analysis by the imposed parabolic approximation should be assessed. This is primarily manifested in the computed entrainment velocity distribution on the injection plane and in the resultant nearfield induced pressure distribution.

5. The developed interaction algorithm should be critically evaluated for potential simplification to yield an entrainment model applicable to a computationally-elementary strictly potential flow analysis.

61

REFERENCES

1. Chang, H.-C., "The Roll-Up of A Cylindrical Jet in A Cross-Flow," Aerospace Research Laboratories Report ARL 73-0131, 1973.

2. Wooler, P. T., "Development of An Analytical Model for the Flow of A Jet Into A Subsonic Cross-Wind," NASA SP-218, p. 101-118, 1968.

3. Schmidt, H., "Deflection of A Round Turbulent Jet in A Cross-Wind," Arch. Mech., Vol. 26, Pt. 5, p. 849-859, 1974.

4. Jordinson, R., "Flow in A Jet Directed Normal to the Wind," ARC Report and Memoranda No. 3074, 1956.

5. Moussa, A. F., Trischka, J. W. and Eskinazi, F., "The Near Field in the Mixing of A Round Jet with A Cross Stream," J. Flu. Mech., Vol. 80 Pt. 1, p. 49-80, 1977.

6. Vogler, R. D., "Surface Pressure Distributions Induced on A Flat Plate by A Cold Air Jet Issuing Perpendicularly from the Plate and Normal to A Low-Speed Free Stream Flow,' NASA TN D-1629, 1963.

7. Bradbury, L. J. S., and Wood, M. N., "The Static Pressure Distribution Around A Circular Jet Exhausting Normally from A Plane Wall into an Airstream," C. P. No. 822, 1965, British Aero. Res. Council.

8. McMahon, H. M. and Mosher, D. K., "Experimental Investigation of Pressures Induced on A Flat Plate by A Jet Issuing into A Subsonic Crosswind", NASA SP-218, p. 49-62, 1968.

9. Margason, R. J. and Fearn, R., "Jet-Wake Characteristics and Their Induced Aerodynamic Effects on V/STOL Aircraft in Transition Flight," NASA SP-218, p. 1-18, 1968.

10. Mosher, D. K., "An Experimental Investigation Of A Turbulent Jet In A Cross-Flow," Aerospace Engineering Report No. 70-7, Georgia Institute Of Technology, 1970.

11. Kamotani, Y. and Greber, I., "Experiments On A Turbulent Jet In A Cross-Flow," AIAA J., Vol. 10, No. 11, p. 1425-29, 1972.

12. Fearn, R. & Weston, R. P., "Vorticity Associated With A Jet In A Cross-Flow," AIAA J., Vol. 12, No. 12, p. 1666-1671, 1974.

13. Fearn, R. L. and Weston, R. P., "Induced Pressure Distributions Of A Jet In A Cross-Flow," NASA TN-D-7916, 1976.

14. Thames, F. C. and Weston, R. P., "Properties of Aspect-Ratio 4.0 Rectangular Jets In A Subsonic Crossflow," AIAA Paper No. 78-1508, 1978.

15. Kotansky, D. R. and Bower, W. W., "Forces and Moments Produced On A Two-Dimensional Body In A Strong Lift-Jet/Airframe/Ground Interaction," AD-A024 022, Vol. I, p. 288-303, 1975.

16. Kotansky, D. R., Durando, N. A., Bristow, D. R., and Saunders, P. W., "Multi-Jet Induced Forces and Moments on VTOL Aircraft Hovering In and Out of Ground Effect," NADC Report 77-229-30, 1977.

17. Bower, W. W. and Kotansky, D. R., "A Navier-Stokes Analysis of the Two-Dimensional Ground Effects Problem," AIAA Paper No. 76-621, 1976.

18. Bower, W. W., "Viscous Flow Simulations in VTOL Aerodynamics," in Future Computer Requirements for Computational Aerodynamics, NASA CP-2032, p. 154-167, 1977.

19. Walters, M. and Henderson, C., "V/STOL Aerodynamics Technology Assessment," NADC Report No. 77272-60, 1978.

20. Baker, A. J., Finite Element Computational Fluid Mechanics, University of Tennessee, Manuscript, 1978.

21. Baker, A. J., Manhardt, P. D. and Orzechowski, J. A., "A Numerical Solution Algorithm for Prediction of Turbulent Aerodynamic Corner Flows," AIAA Paper No. 79-0073, 1979.

22. Baker, A. J. and Manhardt, P. D., "Finite Element Analysis of Low-Speed Viscous and Inviscid Aerodynamic Flows," NASA CR-2908, 1977.

23. Bathe, K. J., et al., "SAP-IV: A Structural Analysis Program for Static and Dynamic Response of Linear Systems," Dept. Civil Engineering Report PB-221 967, U. Calif., June 1973.

APPENDIX

THE THREE-DIMENSIONAL PARABOLIC

NAVIER-STOKES EQUATIONS

The description of a state point in multi-dimensional fluid mechanics is contained within solution of a coupled nonlinear partial differential equation system describing conservation of mass, momentum and energy. Unique solutions are obtained upon closure by specification of constitutive behavior and boundary conditions. In Cartesian tensor notation, the non-dimensional conservation form of the Navier-Stokes equation system is

$$L(\rho) \equiv \frac{\partial \rho}{\partial t} + \frac{\partial}{\partial x_j}(\rho u_j) = 0 \tag{A.1}$$

$$L(\rho \dot{u}_i) \equiv \frac{\partial}{\partial t}(\rho u_i) + \frac{\partial}{\partial x_j}\left[\rho u_j u_i + p\delta_{ij} - Re^{-1}\sigma_{ij}\right] + \rho b_i = 0 \tag{A.2}$$

$$L(\rho H) \equiv \frac{\partial}{\partial t}(\rho H) + \frac{\partial}{\partial x_j}\left[\rho u_j H - (\gamma - 1)M_\infty^2 Re^{-1}\sigma_{ij}u_i - Re^{-1}Pr^{-1}\mu\frac{\partial H}{\partial x_j}\right]$$
$$- (\gamma - 1)M_\infty^2\frac{\partial p}{\partial t} = 0 \tag{A.3}$$

The dependent variable in equations (A.1)-(A.3) have their usual interpretation in fluid mechanics, i.e., ρ is mass density, u_j is the velocity vector, p is the static pressure, b is a body force, and H is the stagnation enthalpy. Furthermore, σ_{ij} is the Stokes stress tensor, defined as

$$\sigma_{ij} \equiv \mu\left[\frac{\partial u_i}{\partial x_j} + \frac{\partial u_j}{\partial x_i}\right] - \frac{2\mu}{3}\frac{\partial u_k}{\partial x_k}\delta_{ij} \tag{A.4}$$

where μ is the dynamic viscosity. The equation of state for a perfect gas closes the definition.

Equations (A.1)-(A.4) are valid for both laminar and turbulent flows. Their solution for the latter becomes tractible in a practical sense only after time-averaging. Mass-weighted time-averaging is employed and the Reynolds decomposition is (ref. A.1)

$$u_j(x_i,t) \equiv \tilde{u}_j(x_i) + u_j''(x_i,t) \tag{A.5}$$

The mass-weighted time-average velocity is defined as

$$\tilde{u}_j \equiv \overline{\rho u_j}/\bar{\rho} \tag{A.6}$$

and

$$\overline{\rho u_i'} \equiv \lim_{T \to \infty} \int_t^{t+T} (\rho u_i - \bar{\rho}\tilde{u}_i) dt \equiv 0 \tag{A.7}$$

This operation yields the important relations

$$\overline{\rho u_i u_j} = \bar{\rho}\tilde{u}_i\tilde{u}_j + \overline{\rho u_i' u_j'} \tag{A.8}$$

$$\tilde{H} = \tilde{h} + \frac{1}{2}\tilde{u}_i\tilde{u}_i + \frac{1}{2}\overline{\rho u_i' u_i'}/\bar{\rho} \tag{A.9}$$

Substitution of equations (A.5)-(A.6) into (A.1)-(A.4), time-averaging and collecting terms yields the time-averaged Navier-Stokes equation system

$$L(\bar{\rho}) = \frac{\partial \bar{\rho}}{\partial t} + \frac{\partial}{\partial x_j}[\tilde{u}_j\bar{\rho}] = 0 \tag{A.10}$$

$$L(\bar{\rho}\tilde{u}_i) = \frac{\partial(\bar{\rho}\tilde{u}_i)}{\partial t} + \frac{\partial}{\partial x_j}\left[\tilde{u}_j(\bar{\rho}\tilde{u}_i) + \bar{p}\delta_{ij} - \bar{\sigma}_{ij} + \overline{\rho u_i' u_j'}\right] = 0 \tag{A.11}$$

$$L(\bar{\rho}\tilde{H}) = \frac{\partial(\bar{\rho}\tilde{H})}{\partial t} + \frac{\partial}{\partial x_j}\left[\tilde{u}_j(\bar{\rho}\tilde{H}) + \overline{\rho H' u_j'} - (\gamma - 1)M_\infty^2 Re\left[\tilde{u}_i\bar{\sigma}_{ij} + \overline{u_i'\sigma_{ij}}\right]\right.$$

$$\left. - Re^{-1}Pr^{-1}\bar{\mu}\frac{\partial\tilde{H}}{\partial x_j}\right] - (\gamma - 1)M_\infty^2\frac{\partial\bar{p}}{\partial t} = 0 \tag{A.12}$$

The three-dimensional parabolic Navier-Stokes (3DPNSO) equations are established from equations (A.10)-(A.12) under the assumptions that:

(1) A predominant mean flow direction is uniformly discernible.

(2) In this direction (only) diffusion processes are negligible compared to convection, and,

(3) Overall three-dimensional elliptic character is provided by interaction with the potential freestream flow.

The parabolic approximation to equations (A.11)-(A.12) basically constrains summation limits. Assuming the x_1 coordinate aligned with the direction of predominant flow, the parabolic approximation is concisely expressed as

$$\bar{\sigma}_{ij} = \frac{\bar{\mu}}{Re}(1 - \delta_{j1})\left[\frac{\partial\tilde{u}_i}{\partial x_j} + \frac{\partial\tilde{u}_j}{\partial x_i} - \frac{2}{3}\frac{\partial\tilde{u}_k}{\partial x_k}\delta_{ij}\right] \tag{A.13}$$

65

The subscript bar notation denotes the index not eligible for the summation convention, but identical with the value of the synonymous tensor index. The parabolic approximation to equation (A.12) also requires eliminating the x_1 component of the diffusion terms involving the time-averaged viscosity $\bar{\mu}$. The parabolization procedure effectively removes the boundary value character on the x_1 coordinate from the equations.

The 3DPNS equation system becomes closed upon identification of the components of the Reynolds stress tensor. Baker (ref. A.2) has developed a constitutive equation for the kinematic Reynolds stress tensor - $\overline{u_i' u_j'}$ as

$$- \overline{u_i' u_j'} = -k\alpha_{ij} + C_4 \frac{k^2}{\varepsilon} \left[\frac{\partial \tilde{u}_i}{\partial x_j} + \frac{\partial \tilde{u}_j}{\partial x_i} \right] + C_2 C_4 \frac{k^3}{\varepsilon^2} \left[\frac{\partial \tilde{u}_i}{\partial x_k} + \frac{\partial \tilde{u}_k}{\partial x_i} \right]\left[\frac{\partial \tilde{u}_k}{\partial x_j} + \frac{\partial \tilde{u}_j}{\partial x_k} \right] + \ldots \tag{A.14}$$

This expansion results from reexpression of triple correlations within the Reynold's stress transport equation using the model of Launder, Reece and Rodi (ref. A.3), and is a generalization of the original analysis by Gessner and Emery (ref. A.4). In equation (A.14) α_{ij} is the diagonal tensor

$$\alpha_{ij} = \frac{1}{3k} (\overline{u_\ell' u_\ell'}) a_{\underline{i}} \delta_{ij} \tag{A.15}$$

and equation (A.14) represents an anisotropic tensor. In equation (A.15) the a_i are the coefficients that admit anisotropy and $a_1 \equiv C_1$ $a_2 = a_3 = C_3$ is suggested, where the C_i are functions in terms of two "universal" empirical constants derived by Hanjalic and Launder (ref. A.5). Additionally, k is the kinetic energy of the turbulence velocity field

$$k \equiv \frac{1}{2} \overline{u_i' u_i'} \tag{A.16}$$

and ε is the isotropic dissipation function defined by the contraction

$$\frac{2}{3} \delta_{ij} \varepsilon \equiv 2\bar{\nu} \frac{\overline{\partial u_i' \partial u_j'}}{\partial x_k \partial x_k} \tag{A.17}$$

The governing differential equations for k and ε are (ref. A.1)

$$L(k) = \frac{\partial k}{\partial t} + \frac{\partial}{\partial x_j} \left[\tilde{u}_j k - \left(C_k \frac{k}{\varepsilon} \overline{u_i' u_j'} + \bar{\nu} \delta_{ij} \right) \frac{\partial k}{\partial x_i} \right]$$

$$+ \overline{u_i' u_j'} \frac{\partial \tilde{u}_i}{\partial x_j} + \varepsilon = 0 \tag{A.18}$$

66

$$L(\varepsilon) = \frac{\partial \varepsilon}{\partial t} + \frac{\partial}{\partial x_j} \left[\tilde{u}_j \varepsilon - C_\varepsilon \frac{k}{\varepsilon} \overline{u_i' u_j'} \frac{\partial \varepsilon}{\partial x_i} \right]$$

$$+ C_\varepsilon^1 \overline{u_i' u_j'} \frac{\varepsilon}{k} \frac{\partial \tilde{u}_i}{\partial x_j} + C_\varepsilon^2 \frac{\varepsilon^2}{k} = 0 \qquad (A.19)$$

The various C_k and C_ε^α are empirical model constants.

The 3DPNS equation system is obtained by deletion of the time derivatives in equations (A.10)-(A.11) and (A.18)-(A.19) and eliminating the x_1 stress components in equation (A.14) in the manner illustrated for the Stoke's stress tensor. The resultant 3DPNS equation system for isoenergetic flow is

$$L(\bar{\rho}) = \frac{\partial}{\partial x_i} (\bar{\rho} \tilde{u}_i) = 0 \qquad (A.20)$$

$$L(\bar{\rho} \tilde{u}_1) = \frac{\partial}{\partial x_i} (\bar{\rho} \tilde{u}_i \tilde{u}_1) + \frac{\partial \bar{p}}{\partial x_1} - \frac{\partial}{\partial x_\ell} \left[\frac{\bar{\mu}}{Re} \frac{\partial \tilde{u}_1}{\partial x_\ell} - \overline{\rho u_1' u_\ell'} \right] = 0 \qquad (A.21)$$

$$L(\bar{\rho} \tilde{u}_2) = \frac{\partial}{\partial x_i} (\bar{\rho} \tilde{u}_i \tilde{u}_2) + \frac{\partial \bar{p}}{\partial x_2} - \frac{\partial}{\partial x_\ell} \left[\frac{\bar{\mu}}{Re} \left(\frac{\partial \tilde{u}_2}{\partial x_\ell} + \frac{\partial \tilde{u}_\ell}{\partial x_2} \right) - \overline{\rho u_2' u_\ell'} \right] = 0 \qquad (A.22)$$

$$L(\bar{\rho} \tilde{u}_3) = \frac{\partial}{\partial x_i} (\bar{\rho} \tilde{u}_i \tilde{u}_3) + \frac{\partial \bar{p}}{\partial x_3} - \frac{\partial}{\partial x_\ell} \left[\frac{\bar{\mu}}{Re} \left(\frac{\partial \tilde{u}_3}{\partial x_\ell} + \frac{\partial \tilde{u}_\ell}{\partial x_3} \right) - \overline{\rho u_3' u_\ell'} \right] = 0 \qquad (A.23)$$

$$L(k) = \frac{\partial}{\partial x_i} (\bar{\rho} \tilde{u}_i k) - \frac{\partial}{\partial x_i} \left[\bar{\rho} \left(\frac{\bar{\nu}}{Re} + C_k \frac{k}{\varepsilon} \overline{u_i' u_k'} \right) \frac{\partial k}{\partial x_k} \right] + \overline{\rho u_i' u_k'} \frac{\partial \tilde{u}_k}{\partial x_i} + \bar{\rho} \varepsilon = 0 \qquad (A.24)$$

$$L(\varepsilon) = \frac{\partial}{\partial x_i} (\bar{\rho} \tilde{u}_i \varepsilon) - \frac{\partial}{\partial x_i} \left[\bar{\rho} \left(0 + C_\varepsilon \overline{u_i' u_k'} \frac{k}{\varepsilon} \right) \frac{\partial \varepsilon}{\partial x_k} \right]$$

$$+ C_\varepsilon^1 \overline{\rho u_i' u_\ell'} \frac{\varepsilon}{k} \frac{\partial \tilde{u}_k}{\partial x_\ell} + C_\varepsilon^2 \bar{\rho} \varepsilon^2 k^{-1} = 0 \qquad (A.25)$$

67

These equations introduce the 3DPNS limited summation index convention $1 \leq i, j \leq 3$, $2 \leq k, \ell \leq 3$. The dilitation term in the Stoke's stress tensor has been deleted from equations (A.21)-(A.23) as neglibibly small.

The parabolic approximation to equation (A.14) is used in completing terms in equations (A.21)-(A.25), yielding

$$\overline{u_1' u_1'} = C_1 k$$

$$\overline{u_2' u_2'} \equiv C_3 k - 2C_4 \frac{k^2}{\epsilon} \frac{\partial \tilde{u}_2}{\partial x_2} \qquad - C_2 \frac{k}{\epsilon} C_4 \frac{k^2}{\epsilon} \left(\frac{\partial \tilde{u}_1}{\partial x_2} \right)^2$$

$$\overline{u_3' u_3'} = C_3 k - 2C_4 \frac{k^2}{\epsilon} \frac{\partial \tilde{u}_3}{\partial x_3} \qquad - C_2 \frac{k}{\epsilon} C_4 \frac{k^2}{\epsilon} \left(\frac{\partial \tilde{u}_1}{\partial x_3} \right)^2$$

$$\overline{u_1' u_2'} = \qquad - C_4 \frac{k^2}{\epsilon} \frac{\partial \tilde{u}_1}{\partial x_2}$$

$$\overline{u_1' u_3'} = \qquad - C_4 \frac{k^2}{\epsilon} \frac{\partial \tilde{u}_1}{\partial x_3}$$

$$\overline{u_2' u_3'} = \qquad - C_4 \frac{k^2}{\epsilon} \left[\frac{\partial \tilde{u}_2}{\partial x_3} + \frac{\partial \tilde{u}_3}{\partial x_2} \right] - C_2 \frac{k}{\epsilon} C_4 \frac{k^2}{\epsilon} \frac{\partial \tilde{u}_1}{\partial x_2} \frac{\partial \tilde{u}_1}{\partial x_3} \qquad \text{(A.26)}$$

For equation (A.21), the divergence term becomes

$$\frac{\partial}{\partial x_\ell} \left[\frac{\bar{\mu}}{Re} \frac{\partial \tilde{u}_1}{\partial x_\ell} - \overline{\rho u_1' u_\ell'} \right] = \frac{\partial}{\partial x_\ell} \left[\left(\frac{\bar{\mu}}{Re} + C_4 \frac{\bar{\rho} k^2}{\epsilon} \right) \frac{\partial \tilde{u}_1}{\partial x_\ell} \right] \qquad \text{(A.27)}$$

Defining the "effective" kinematic viscosity

$$\nu^e \equiv \frac{\bar{\nu}}{Re} + C_4 \left(\frac{k}{\epsilon} \right) k \qquad \text{(A.28)}$$

equation (A.28) becomes

$$\left[\frac{\bar{\mu}}{Re} \frac{\partial \tilde{u}_1}{\partial x_\ell} - \overline{\rho u_1' u_\ell'} \right] = \frac{\partial}{\partial x_\ell} \left[\bar{\rho} \nu^e \frac{\partial \tilde{u}_1}{\partial x_\ell} \right] \qquad \text{(A.29)}$$

In the transverse flow momentum equations (A.22)-(A.23), the divergence terms become

68

$$\frac{\partial}{\partial x_\ell}\left[\frac{\bar{\mu}}{Re}\left(\frac{\partial \tilde{u}_k}{\partial x_\ell} + \frac{\partial \tilde{u}_\ell}{\partial x_k}\right) - \overline{\rho u_k' u_\ell'}\right] = \frac{\partial}{\partial x_\ell}\left[\bar{\rho}\nu^e\left(\frac{\partial \tilde{u}_k}{\partial x_\ell} + \frac{\partial \tilde{u}_\ell}{\partial x_k}\right)\right]$$

$$- \frac{\partial}{\partial x_\ell}\left[\bar{\rho}k a_{\underline{k\ell}} - \bar{\rho}C_2\frac{k}{\epsilon}C_4\frac{k}{\epsilon}k\frac{\partial \tilde{u}_1}{\partial x_k}\frac{\partial \tilde{u}_1}{\partial x_\ell}\right] \tag{A.30}$$

The first right-hand term is basically identical to equation (A.28) for $\tilde{u}_1$, with the addition of terms involving shear of the alternative transverse plane mean velocity component $\tilde{u}_\ell$. The second term is a non-homogeneity involving shear components of the predominant velocity $\tilde{u}_1$ which acts as a source term within the transverse momentum equations.

The divergence term common to both the k and ϵ equations becomes,

$$\frac{\partial}{\partial x_i}\left[C_q\bar{\rho}\frac{k}{3\epsilon}\overline{u_i' u_\ell'}\frac{\partial q}{\partial x_\ell}\right] = \frac{\partial}{\partial x_\ell}\left[\frac{2}{3}C_q\bar{\rho}\frac{k^2}{\epsilon}\frac{\partial q}{\partial x_\ell}\right] \tag{A.31}$$

where q represents eigher k or ϵ, and is identical to the Reynold's stress contribution in equation (A.28) with C_4 replaced by C_q. The production terms for both k and ϵ are basically identical, with the latter multiplied by $C_\epsilon^1\frac{k}{\epsilon}$.

The Reynold's stress-velocity shear contraction under the parabolic approximation becomes

$$\overline{\rho u_i' u_k'}\frac{\partial \tilde{u}_i}{\partial x_k} = \bar{\rho}C_4\frac{k^2}{\epsilon}\left[\frac{\partial \tilde{u}_1}{\partial x_\ell}\frac{\partial \tilde{u}_1}{\partial x_\ell}\right] + 2\bar{\rho}C_2\frac{k}{\epsilon}C_4\frac{k}{\epsilon}k\left(\frac{\partial \tilde{u}_1}{\partial x_1}\right)\left[\frac{\partial \tilde{u}_1}{\partial x_\ell}\frac{\partial \tilde{u}_1}{\partial x_\ell}\right] \tag{A.32}$$

The key element of a viscous-inviscid interaction algorithm is the pressure coupling between the two flowfield descriptions. Derivation of the pressure coupling algorithm employs the steady parabolized mean flow momentum equations (A.21)-(A.23), and is based on the two-dimensional transverse plane Poisson equation obtained by application of the divergence operator. Recalling the limited summation convention, $1 \leq j \leq 3$, and $2 \leq k, \ell \leq 3$,, this equation is

$$L(\bar{p}) = \frac{\partial}{\partial x_\ell}\left[\frac{\partial \bar{p}}{\partial x_\ell} + \frac{\partial}{\partial x_j}(\bar{\rho}\tilde{u}_j\tilde{u}_\ell) - \frac{\partial}{\partial x_k}(\bar{\sigma}_{\ell k} - \overline{\rho u_\ell' u_k'})\right] = 0 \tag{A.33}$$

The algorithm is based upon the observation that the solution of a linear, elliptic Poisson equation consists of a complementary and a particular contribution as

$$\bar{p}(x_i) = p_c(x_i) + p_p(x_i) \tag{A.34}$$

By definition, the complementary solution satisfies the homogeneous form
of equation (A.33), i.e.

$$L(p_c) = \frac{\partial^2 p_c}{\partial x_\ell^2} = 0 \tag{A.35}$$

subject to the known boundary conditions for $\bar{p}(x_j)$. Since the bounding
inviscid flow pressure distribution is assumed everywhere known,

$$\bar{p}(\bar{x}_\ell) = p^I(\bar{x}_\ell) \tag{A.36}$$

In equation (A.36), $\bar{x}_\ell$ indicates x_ℓ constrained to the boundary of the
viscous solution domain, $\partial\Omega = \partial R^2 \times x_1$, and p^I is the (inviscid flow) pressure
level distribution. Elsewhere on $\partial\Omega$, the appropriate boundary condition is
vanishing normal gradient, i.e.

$$\ell(p_c) = \frac{\partial}{\partial x_\ell} p_c \cdot \hat{n}_\ell = 0 \tag{A.37}$$

The particular solution p_p is any function satisfying equation (A.33)
with homogeneous boundary conditions on closure segments of Ω coincident with
p^I known. Elsewhere, the boundary condition for p_p is established from the
inner product of the parent steady momentum equations (A.22)-(A.23) with the
closure surface normal. Since the convection term vanishes identically at a
wall or symmetry plane,

$$\ell(p_p) + \frac{\partial p}{\partial x_\ell} \hat{n}_\ell - \frac{\partial}{\partial x_k} \left[\bar{\sigma}_{\ell k} - \overline{\rho u_k' u_\ell'} \right] \hat{n}_\ell = 0 \tag{A.38}$$

The appropriate Poisson equation for p_p is the inviscid form, (ref. A.6)

$$L(p_p) = \frac{\partial}{\partial x_\ell} \left[\frac{\partial p_p}{\partial x_\ell} + \frac{\partial}{\partial x_j} \left(\bar{\rho}\tilde{u}_j\tilde{u}_\ell + \overline{\rho u_\ell' u_k'} \right) \right] = 0 \tag{A.39}$$

Equations (A.33)-(A.39) define the algorithm for determination of pressure
distributions in the three-dimensional parabolic viscous flow solution. The
x_1 pressure gradient used in solution of the predominant flow momentum equation
is determined solely from the complementary pressure solution. The complemen-
tary and particular solutions are summed, as in the defining equation, and
differentiated to form the transverse pressure gradient field. The continuity
equation (A.20) is substituted directly into the right side of equation (A.39).

Appendix References

A.1 Cebeci, T. and Smith, A.M.O., _Analysis Of Turbulent Boundary Layers_, Academic Press, New York, 1974.

A.2 Baker, A. J., "A Reynolds Stress Constitutive Equation For Parabolic Three-Dimensional Turbulent Flows," Manuscript, 1978.

A.3 Launder, B. E., Reece, G. J. and Rodi, W., "Progress In The Development Of A Reynolds-Stress Turbulence Closure," J. Flu. Mech., V. 68, Pt. 3 pp. 537-566, 1975.

A.4 Gessner, F. B., and Emery, A. F., "A Reynolds Stress Model For Turbulent Corner Flows - Pt. I: Development Of The Model," J. Flu. Engr. Trans. ASME, pp. 261-268, 1976.

A.5 Hanjalic, K. and Launder, B. E., "A Reynolds Stress Model Of Turbulence And Its Application To Thin Shear Flows," J. Flu. Mech., V. 52, Pt. 4, pp. 609-638, 1972.

A.6 Baker, A. J., _Finite Element Computational Fluid Mechanics_, University of Tennessee, Manuscript, 1978.

AIRCRAFT AND CREW SYSTEMS TECHNOLOGY DIRECTORATE

6053:KY
28 DEC 1978

DISTRIBUTION LIST

Commander
Naval Weapons Center
China Lake, CA 93555

Director
National Aeronautics & Space Administration
Ames Research Center
Moffett Field, CA 94035
Attn: S. Anderson

Commanding Officer
Naval Air Propulsion Center
Trenton, NJ 08628

Director
National Aeronautics & Space Administration
Flight Research Center
Edwards Air Force Base, CA 93523

Commander
Naval Air Test Center
Patuxent River, MD 20670

Director
National Aeronautics & Space Administration
Langley Research Center
Hampton, VA 23365

Commander
David Taylor Naval Ship Research
 & Development Center
Bethesda, MD 20034

Director
National Aeronautics & Space Administration
Lewis Research Center
21000 Brooke Park Road
Cleveland, OH 44135

Chief
Office of Naval Research
800 N. Quincy Street
Arlington, VA 22217

Director
Air Force Flight Dynamics Laboratory
 (ASD/ENFDH)
Wright-Patterson Air Force Base
Dayton, OH 45433

Institute of Defense Analysis
400 Army Navy Drive
Arlington, VA 22202
Attn: J. Attinello

Commander
Air Force Aeronautical Systems Division
Wright-Patterson Air Force Base
Dayton, OH 45433

Rockwell International
Los Angeles, CA 90053

General Dynamics Corporation
Ft. Worth, TX 76108

Fairchild-Republic Corporation
Farmingdale, Long Island, NY 11735

Hughes Aircraft Company
Culver City, CA 90230

Royal Aeronautical Establishment
Bedford, England
Attn: A. Woodfield

72

Superintendent
Naval Postgraduate School
Monterey, CA 93940

Commander
Air Force Flight Test Center
Edwards Air Force Base, CA 93523

Commanding Officer
Army Aviation Systems Test Activity
Edwards Air Force Base, CA 93523

Administrator
Defense Documentation Center for
 Scientific & Technical Information (DDC)
Building #5, Cameron Station
Alexandria, VA 22314
(12 copies)

Commanding General
Army Aviation Systems Command
St. Louis, MO 63102

Office of Naval Research
800 N. Quincy Street
Arlington, VA 22214
Attn: Dr. R. Whitehead

Commander
Naval Air Systems Command (AIR-954)
Department of the Navy
Washington, D.C. 20361
(7 copies: (2) for retention
            (2) for AIR-320D
            (1) for AIR-5301
            (1) for PMA-257
            (1) for AIR-03PA)

Commander
Naval Air Development Center
Warminster, PA 18974
(13 copies: (3) for Code 813
            (10) for Code 6053)

General Dynamics
Convair Division
P.O. Box 80986
San Diego, CA 92138

General Electric Company
Aircraft Engine Group
1000 Western Avenue
Lynn, MA 01910

McDonnell-Douglas Corporation
P.O. Box 516
St. Louis, MD 63166

McDonnell-Douglas Corporation
3855 Lakewood Boulevard
Long Beach, CA 90808

Lockheed-California Company
P.O. Box 551
Burbank, CA 91503

Pratt & Whitney Aircraft Division
Division of United Aircraft Corporation
East Hartford, CT 06108

The Boeing Company
Seattle, WA 98101

Northrop Corporation
Hawthorne, CA 90250

LTV Aerospace Corporation
Dallas, TX 75221

Lockheed-Georgia Company
Marietta, GA 30061

Rockwell International
Columbus, OH 43216

Grumman Aerospace Corporation
Bethpage, Long Island, NY 11714